

**Assessing the Vulnerability of Small-Scale Water Resources  
Using High Spatial Resolution Remote Sensing**

by

Sammy Al-Khalifa

B.Sc., The University of British Columbia, 2019

A THESIS SUBMITTED IN PARTIAL FULFILLMENT OF  
THE REQUIREMENTS FOR THE DEGREE OF

MASTER OF SCIENCE

in

THE FACULTY OF GRADUATE AND POSTDOCTORAL STUDIES  
(FORESTRY)

THE UNIVERSITY OF BRITISH COLUMBIA

(Vancouver)

January 2023

© Sammy Al-Khalifa, 2023

The following individuals certify that they have read, and recommend to the Faculty of Graduate and Postdoctoral Studies for acceptance, the thesis entitled:

Assessing the Vulnerability of Small-Scale Water Resources Using High Spatial Resolution Remote Sensing

---

submitted by Sammy Al-Khalifa in partial fulfilment of the requirements for

the degree of Master of Science

---

in Forestry

---

**Examining Committee:**

Dr. Sarah E. Gergel, Professor, Department of Forest and Conservation Sciences, UBC  
Supervisor

Dr. Nicholas Coops, Professor, Department of Forest Resources Management, UBC  
Supervisory Committee Member

Dr. Mark Johnson, Professor, Department of Earth, Ocean and Atmospheric Sciences, UBC  
Supervisory Committee Member

Dr. Naomi Schwartz, Professor, Department of Geography, UBC  
Additional Examiner

## Abstract

Water stress due to physical scarcity and poor water quality impacts billions of people worldwide. Internationally, an important goal of the United Nations' Sustainable Development Goals (SDGs) is the improvement of ambient water quality by tracking the proportion of inland water bodies with acceptable water quality. Thus, there is a global, pressing need for fast, reliable, and accessible ways to monitor the water quality in small inland water bodies. In this research, I evaluate the utility of high spatial resolution remote sensing for monitoring water quality constituents (Chlorophyll-a and turbidity) in small reservoirs (0.01 km<sup>2</sup>) in southwestern Kenya.

First, I used a novel combination of remote sensing indices and landscape features to build statistically robust empirical models of water quality parameters that were measured in situ. I then used these models to extrapolate water quality in 60 reservoirs over 43 consecutive months (2019-July 2022) across a land-use gradient. These results were then used to examine patterns in water quality across space and time. Finally, I used high spatial resolution imagery to quantify the areal change (or drying out) of reservoirs throughout a single dry season.

Overall, Sentinel-2 satellite imagery produced better models of Chl-a ( $R^2 = 0.66$ ) when compared to PlanetScope imagery which produced more accurate maps of turbidity ( $R^2 = 0.72$ ). Furthermore, introducing landscape features such as land cover, maximum reservoir size, and proximity to roads improved the statistical power of models by as much as 9%. Turbidity was marginally significantly different in reservoirs across the land-use gradient, with the transition zone having the most turbid reservoirs. From 2019 to 2022, Chl-a and turbidity have been steadily improving in 46% and 40% of reservoirs, respectively. Notably, Chl-a concentrations

have been improving more rapidly in the cropland zone. Additionally, nearly half of reservoirs lost over 50% of their surface area during the 2021 dry season, a period of exceptionally intense drought; whereas a quarter of all reservoirs dried out completely. This research has the potential to help support monitoring and planning within the water resources sector by prioritizing the use of climate resilient infrastructure such as water pans.

## **Lay Summary**

Access to safe, reliable water is a challenge across the globe. Small water bodies (both natural and man-made) serve as sustainable, low-cost sources of water in many East African countries. However, these water bodies are vulnerable to poor water quality as well as drought. My thesis aims to quantify these vulnerabilities by combining satellite imagery and landscape features to estimate the water quality of small water bodies in Narok, Kenya. I then use these water quality estimations to examine the effects of neighboring land-use on water quality. I found the water quality of most reservoirs has been improving from 2019-2022, especially in agricultural areas. Across all water bodies studied, most shrank and/or dried out completely during the dry season. These methods can be used to assess patterns of vulnerability in small water bodies across semi-arid regions, and provide a fast, cost-effective alternative to traditional water quality assessment methods.

## **Preface**

This thesis is based on the original, independent research conducted by myself in Dr. Sarah E. Gergel's Landscape Ecology lab. Dr. Sarah Gergel and I conceptualized the study design after multiple discussions with our collaborators at the Maasai Mara University in Narok Kenya. Dr. Romulus Abila and Dr Samson Mabwoga provided context and guidance on conducting research in Narok and were also responsible for carrying out all field measurements along with Simo Raphael Ongaya. I was responsible for building all models and conducting all analyses. I wrote the manuscript with editorial assistance from Dr. Gergel, Dr Nicholas Coops and Dr Mark Johnson.

# Table of Contents

<b>Abstract .....</b>	<b>iii</b>
<b>Lay Summary.....</b>	<b>v</b>
<b>Preface.....</b>	<b>vi</b>
<b>Table of Contents.....</b>	<b>vii</b>
<b>List of Tables .....</b>	<b>ix</b>
<b>List of Figures .....</b>	<b>xi</b>
<b>Acknowledgements .....</b>	<b>xiv</b>
<b>Chapter 1: Introduction.....</b>	<b>1</b>
1.1 Challenges Facing Water Resources.....	1
1.2 History of Water Quality Monitoring.....	2
1.3 Technical Background on Remote Sensing of Water Quality .....	5
1.4 Remaining Research Gaps in the Remote Sensing of Small Water Bodies.....	8
1.5 Research Objectives .....	9
<b>Chapter 2: Methods .....</b>	<b>11</b>
2.1 Introduction .....	11
2.2 Methods .....	13
2.2.1 Description of Study Region .....	13
2.2.2 Methods Overview.....	16
2.2.3 In situ Water Quality Sampling (Chlorophyll-a and Turbidity) .....	18
2.2.4 Satellite Imagery and Band Selection .....	21
2.2.5 Landscape Features.....	25
2.2.6 Statistical Analyses (Model Building and Comparison) .....	27
2.2.7 Spatio-Temporal Impacts of Land-use on Water Quality .....	28
2.2.9 Tracking Seasonal Shifts in Reservoir Size.....	30
2.3 Results.....	31
2.3.1 In-situ Samples.....	31
2.3.2 Empirical Water Quality Models.....	32
2.3.3 Landscape Features That Aided Water Quality Estimations .....	36
2.3.4 Spatio-Temporal Trends in Regional Water Quality.....	38
2.3.5 Tracking Seasonal Shifts in Reservoir Size.....	42
<b>Chapter 3: Discussion.....</b>	<b>43</b>
3.1 Key Findings .....	43
3.2 Model Comparisons Demonstrate the Utility of Sentinel-2 and PlanetScope .....	44
3.3 Landscape Features Helped Improve Water Quality Models .....	45
3.4 Regional Spatio-Temporal Trends in Water Quality Across a Land-Use Gradient .....	47
3.5 Tracking Seasonal Shifts in Reservoir Size.....	49

<b>3.6 Limitations</b> .....	<b>51</b>
<b>3.6.1 Spatial Scale and Resolution of Available Information</b> .....	51
<b>3.6.2 Cloud Cover and Atmospheric Correction</b> .....	54
<b>3.6.3 Challenges During a Global Pandemic</b> .....	55
<b>3.7 Implications</b> .....	<b>55</b>
<b>3.7.1 Implication to Remote Sensing Researchers</b> .....	55
<b>3.7.2 Implications for Management in Semi-Arid Regions</b> .....	56
<b>3.8 Future Research</b> .....	<b>58</b>
<b>3.9 Significance and Conclusions</b> .....	<b>59</b>
<b><i>Literature Cited</i></b> .....	<b>61</b>
<b><i>Appendix</i></b> .....	<b>85</b>

## List of Tables

<b>Table 1. Summary of the single bands, ratios and indices investigated to estimate chlorophyll-a and turbidity using Sentinel-2 and Planet imagery. In total, 21 bands, indices, and ratios were investigated for both Chl-a and turbidity. All bands and band combinations were used as explanatory variables in a multiple regression model used to estimate turbidity and Chl-a.</b> .....	25
<b>Table 2. Summary of additional explanatory variables used to fit the Chl-a and turbidity models. Variables with skewed distributions were transformed. Reservoir type refers to whether a reservoir was hand dug or machine excavated. For more information on the datasets used, see Figure 3.</b> .....	27
<b>Table 3. Summary of in situ chlorophyll-a (in Relative Fluorescence Units) and Turbidity (in Nephelometric Turbidity Units) for 30 reservoirs sampled across 3 broad land-use zones in Narok, Kenya. Samples were taken from November 2021 to February 2022. A summary of the mean, median, maximum, and minimum values of chlorophyll-a and turbidity for each reservoir across all months were calculated and included below.</b> .....	32
<b>Table 4. Summary of regression results explaining in-situ water quality as a function of remote sensing indices from two high spatial resolution sensors as well as other landscape variables (described in Figure 3). February sub-models (ie in-situ measurements and satellite imagery taken during February) were contrasted to global models fit using in situ samples and satellite imagery for all months (Nov 2021 – Feb 2022). Each model (row) was chosen after a forward step-wise selection of variables based on significance (<math>p &lt; 0.05</math>) and AIC score (lowest). Variables with VIF scores higher than 10 were excluded from the final models. February and global models with the highest adjusted <math>R^2</math> values (highlighted in</b>	

grey below) were chosen and used for extrapolation of chlorophyll-a and turbidity to a larger set of 60 reservoirs in the region and are explained in further detail in Table 5. The sample size refers to the number of reservoirs that were sampled in-situ and used to fit the model. For a more detailed version of this table (including AIC and VIF scores), please see Appendix..... 33

**Table 5. Detailed description of the four top models (derived from Table 4) used for extrapolation of chlorophyll-a and turbidity to a larger set of reservoirs in the region. Month-specific Chl-a and turbidity models were fit using measurements taken during a single month (hence N = 30 reservoirs) whereas global models were fit using data from all months (Nov 2021 – Feb 2022) (hence N = 77). Model selection used forward step-wise selection of variables using the lowest Akaike Information Score (AIC) and Value Inflation Factors (VIF) scores less than 10. Please see Tables 1 and 2 for a list of all model variables, and Appendix A.1/A.2 for the full list of models and variables..... 37**

## List of Figures

- Figure 1: Location of Narok county, Kenya, with major towns as well as neighboring counties shown. Located in the southwestern portion of the Great Rift Valley, between the latitudes  $0^{\circ} 50'$  and  $1^{\circ} 50'$  south, Narok county shares a border with Tanzania. Narok county is known for the Maasai Mara National Reserve which transitions into the Serengeti National Park in Tanzania. .... 15**
- Figure 2. Dominant land covers in Narok county, Kenya with three study zones (outlined in boxes) capturing a gradient of land-use from North to South. The northernmost zone is cropland dominated, the middle zone is a transition zone, and the southernmost zone is shrubland dominated. Panels of satellite imagery are available to visualize differences in spatial resolution between the satellite sensors used in the model building. .... 17**
- Figure 3. Input data and methods summary for three research objectives. First, an empirical relationship was established (objective 1) between in situ water quality (from 30 reservoirs) and remote sensing indices (based on PlanetScope and Sentinel-2 imagery), while accounting for land cover (ESRI global 10m map), terrain (Shuttle Radar Topography Mission Digital Elevation Map), and roads (Open Street Map). The strongest empirical models were then used to estimate the water quality of 60 reservoirs across a land-use gradient and used to achieve objective 2. Lastly, the higher resolution PlanetScope imagery (3m) was used to map and quantify the seasonal changes in areal extent in reservoirs (objective 3). .... 18**
- Figure 4. Relationships between in-situ water quality (chlorophyll-a and turbidity) measurements and model-derived estimates of chlorophyll-a and turbidity (using four top**

models from Table 5). Model-derived estimates are based on satellite imagery from Sentinel-2 and PlanetScope corresponding to the day of in situ sampling (+/- 4 days)..... 35

**Figure 5. Partial R<sup>2</sup> values for significant explanatory variables from the top February models for Chl-a and turbidity (Table 5). Explanatory variables included: percent landcover within 100m, elevation, maximum reservoir size, proximity to roads, and four remote sensing band indices (for a list of all explanatory variables and their transformations see Tables 1 and 2). A forward stepwise selection of variables was used to choose variables based on the lowest AIC scores and Value Inflation Factors below 10. The top February models were then used to estimate Chl-a using Sentinel-2 imagery (in black) and turbidity using PlanetScope imagery (in white) in 60 reservoirs. .... 38**

**Figure 6. Patterns of chlorophyll-a and turbidity estimated using remote sensing for 60 reservoirs across a land-use gradient from Zone 1 (agriculture) to Zone 2 (transitional) to Zone 3 (shrublands with little to no agriculture). Land cover was derived using ESRI’s 2020 Global Land Cover Map at 10m spatial resolution. .... 39**

**Figure 7. Water quality trends for 60 small-scale reservoirs across a land-use gradient in Narok, Kenya from January 2019 to July 2022. A nonparametric Mann-Kendall test was used to test for monotonic trends in Chl-a and turbidity for each reservoir. Any reservoir with significant increasing (black dots) and decreasing (white dots) trends in water quality ( $p < 0.05$ ) were further tested using a Sen’s slope estimator to determine where water quality was changing most rapidly (diamond). The highest magnitude of change was calculated as the top 20% of Sen Slopes. .... 41**

**Figure 8. Change in reservoir size across a gradient of agricultural land use. Areal change was mapped using ~3m resolution PlanetScope imagery from the peak of the wet season**

**(June 2021) to the peak of the dry season (Dec 2021). Boundaries were delineated by manual digitization of 60 reservoirs using QGIS software (Hannover version 3.16). Zone 1 is the northern most zone and is dominated by agricultural land covers. Zone 2 is a transition zone containing Agricultural land covers, Shrublands and Forests. Zone 3 is Shrubland dominated with little to no Agricultural land covers. .... 42**

## **Acknowledgements**

Truly this thesis would not have been complete without the support, mentoring, and help of Sarah Gergel, whom I'm sincerely grateful to. I would also like to thank Nicholas Coops and Mark Johnson for their guidance and helpful feedback. A big thank you to all members of the Maasai Mara University for their help in providing context and answering questions (often outside of work hours). Specifically, I would like to thank Dr. Romulus Abila, Dr Samson Mabwoga, Simo Raphael Ongaya, and Jedidah Simantoi. Thank you to my lab mates for their help and moral support: Ingrid Jarvis, Aeryn Ng, Maya Fromstein, and Jen Baron. I would also like to thank Kephra Beckett for her constant support, her hours of editing my writing, and all other help throughout the entire process.

Finally, I would like to thank my family, Esam AlKhalifa, Anna Letz, Saleh AlKhalifa, and Sarah AlKhalifa, for whom I am always grateful.

## **Chapter 1: Introduction**

### **1.1 Challenges Facing Water Resources**

One quarter of the global population is facing extreme water stress (Hofste et al., 2019), with approximately half of humanity experiencing severe water scarcity for at least part of the year (Pörtner et al., 2022). Global freshwater withdrawals have more than doubled since the 1960s (Hofste et al., 2019). Global water use is currently increasing at a steady rate of 1% per year (UNESCO World Water Assessment Programme, 2019), which closely follows the global population growth rate (Department of Economic and Social Affairs, 2019). The scarcity of water is a problem commonly attributed solely to a growing population, however water usage and depletion is better thought of as a function of multiple drivers. Agriculture accounts for approximately 70% of the world's freshwater withdrawals (Döll, 2009; Juliane et al., 2019; Siebert et al., 2010). Socio-economic development and urbanization have also led to increases in the demand for water from energy services and industry (FAO, 2020). Additionally, rising incomes lead to shifts in diets towards more water-intensive foods such as meats and dairy products as nutritional standards increase (FAO, 2020). The scarcity of water is further exacerbated by climate change, which has led to increases in extreme weather events such as droughts (UNESCO World Water Assessment Programme, 2019). The cost of these prolonged periods of water scarcity to societies, ecosystems and economies is disproportionately borne by the most socioeconomically vulnerable (Pörtner et al., 2022). Unfortunately, this phenomenon was highlighted during the onset of the 2020 global pandemic, during which 26% of the global population (approximately 2 billion people) lacked access to safe drinking water services (United Nations, 2021).

In addition to physical scarcity, worsening water quality in many sources of freshwater is a global problem, and further reduces the amount of water that can be safely used. Agriculture is heavily associated with decreased water quality through fertilizer runoff. Fertilizer, drug residues, as well as other types of organic matter from agricultural fields can reach freshwater systems through runoff and leaching (Rosegrant et al., 2017). Such inputs may degrade water quality by increasing diseases, pathogens, and protozoans (such as Giardia and cryptosporidium) which can lead to diarrhea, dysentery, and cholera. Excessive nutrient inputs can also cause eutrophication (Nixon 1995) associated with algal blooms. Blooms of cyanobacteria (also known as Harmful Algal Blooms (HABs)) are toxic and diminish the safety of drinking water for both humans and livestock, as well as have cascading impacts on entire aquatic ecosystems. The drivers of such events are complex, as HABs are difficult to predict (Glibert et al., 2005; Heisler et al., 2008).

Currently, the biggest expansion of agricultural lands is happening in developing countries (Food and Agriculture Organization, 2009). The FAO further suggests that a 70% increase in food production is needed to accommodate population growth by 2050 (Food and Agriculture Organization, 2009). Because this expected expansion of agricultural activity may have negative impacts on provisioning of freshwater, new ways to track, monitor and understand the patterns of water quality and quantity are needed.

## **1.2 History of Water Quality Monitoring**

Robust measures of water quality and quantity are essential to manage water resources in a changing world. Conventionally, water quality measurements in lakes, streams, oceans, and other water bodies necessitated capture of “in situ” measurements, requiring collection of samples in

the field which are then taken into the lab for further analysis. However, in 1970 Clarke et al. found sea surface colour obtained from low-flying aircrafts could be used to estimate chlorophyll concentrations (Clarke et al., 1970). This work fueled decades of new research on the physics of ocean colour remote sensing (Gordon et al., 1975; Gordon & Morel, 1983; Hovis & Leung, 1977) and helped lead to the launch of NASA's Coastal Zone Colour Scanner (CZCS) onboard the Nimbus-7 satellite in 1978. A series of satellite-based ocean colour monitoring sensors have since been deployed, including the Ocean Colour Temperature Scanner (OCTS in 1996), the Sea-viewing Wide field-of-view Sensor (SeaWiFS in 1997), the Moderate Resolution Imaging Spectroradiometer (MODIS in 1999), the Medium Resolution Imaging Spectrometer (MERIS in 2002), the Multispectral Sensor onboard the Sentinel-2 satellites (2015), and more recently the Ocean and Land Colour Instrument onboard the Sentinel-3 satellite (2016). These satellites have been used to quantify a range of water quality constituents including phytoplankton pigments (Chlorophyll-a, phycocyanin), suspended sediments (via Total Suspended Matter and Turbidity), as well as Coloured Dissolved Organic Matter (CDOM).

Despite several technical challenges (discussed further below), remote sensing of water quality in inland water bodies has been successfully undertaken for decades, initially building on advances in marine remote sensing satellites. Bukata et al. (1983) used NASA's CZCS in combination with novel analyses (pioneered by Gordon et al. in 1975) to retrieve chlorophyll-a (Chl-a) in the optically complex waters of Lake Ontario (R. P. Bukata et al., 1983; Gordon et al., 1975). The same satellite was later used to locate upwelling zones and bar fronts in Lake Michigan (Mortimer, 1988). With increasing frequency of imagery from the NASA/USGS Landsat missions, researchers have also been able to reliably estimate total suspended matter,

seston dry weight, water clarity, and high biomass cyanobacteria blooms (Dekker et al., 2001, 2002; Olmanson et al., 2008; Tebbs et al., 2013). Additional satellites such as the Advanced Land Imager (ALI), Hyperion, SeaWiFS, and others have been used to retrieve Secchi depth, Chl-a, CDOM, Tripton, and total phosphorus concentrations (Dekker & Peters, 1993; Kutser et al., 2005; Sun et al., 2014; Verdin, 1985; Wang et al., 2019). Taken together, it is now feasible to retrieve a suite of water quality measurements to characterize the quality and ecological status of water.

More recently, there has been an increase in the use of non-satellite-based technology, such as unmanned aerial vehicles (UAVs) to measure water quality. For example, Prior et al. 2020 was able to retrieve Turbidity and Total Suspended Solids using a UAV with relatively high accuracy (coefficients of determination between 0.85 and 0.92) for a sediment basin in the United States (Prior et al., 2021). A recent review on the use of UAVs in surface water quality monitoring found a marked increase in the frequency of studies using UAVs since 2018 (Sibanda et al., 2021). UAVs offer spatially explicit, and near real time information at fine resolutions. These lightweight systems can be equipped with high resolution multi-spectral cameras, Light Detection and Ranging (Lidar) sensors, infrared sensors and other instruments to monitor water bodies at high spatial resolutions (Beck et al., 2019). Additionally, because UAVs fly at relatively low heights, the acquired imagery does not need atmospheric corrections prior to analysis. However, given their small battery capacity they cannot fly for extended or large distances. Additionally, UAVs require little to no wind to fly safely and are often location-restricted by statutory regulations (Cracknell, 2017; Rhee et al., 2017).

### **1.3 Technical Background on Remote Sensing of Water Quality**

Optical satellite remote sensing uses specialized sensors to measure light reflected off the surface of the earth and the atmosphere. Light (also known as electromagnetic radiation), is composed of photons that travel at different wavelengths and are used to categorize light across the Electromagnetic Spectrum (EM) (Coops & Tooke, 2017; Lillesand & Kiefer, 1979). Only a small portion of light emitted from the sun penetrates our atmosphere (Radio, Infrared, Visible light), and humans can only see an even smaller portion (Visible light). Of particular interest are the Near Infrared (NIR), Short-wave Infrared (SWIR) and Visible portions of the Electromagnetic Spectrum. As these wavelengths are either absorbed or reflected off the surface of the Earth, their unique patterns of absorption and reflection are referred to as the Spectral Signature of an object and can be used for image classification.(Coops & Tooke, 2017; Lillesand & Kiefer, 1979)

Wavelengths around ~ 560 nm correspond to the green portion of the EM. Chlorophyll-a, the dominant pigment in plants responsible for photosynthesis, absorbs light in the Blue and Red portions of the EM, but reflects most of the light in the Green portion, which is the reason humans perceive plants as green (A. A. Gitelson & Merzlyak, 1996). Conversely, wavelengths of ~ 665 nm correspond to the red portion of the EM and is the region where chlorophyll is most highly absorbed (Mishra & Mishra, 2012; H. Yang et al., 2022). Further along the EM is the Near-Infrared (Near-IR) portion (~840 nm) where wavelengths are completely absorbed by water. Any reflectance in the Near-IR region will indicate the presence of particles in the water (H. Yang et al., 2022).

The spectral signatures of optically active constituents (OACs) describe the way in which light is reflected in a water body (Preisendorfer, 1976). These constituents such as CDOM, phytoplankton, nonliving debris (detritus and minerals), and the water itself, all interact with specific wavelengths in predictable ways (Bagheri, 2017; Park & Ruddick, 2005). Satellite sensors measure the amount of light reflected within a narrow range of wavelengths (or “bands”) which can be used to provide estimates of the variety and abundance of different OACs.

Furthermore, the light emitted by the sun and reflected off the surface of OACs (known as “water-leaving radiance”) passes through the atmosphere twice before being recorded by the satellite sensor. The atmosphere itself contains a wide range of particulate matter that interact with photons as they travel, distort the signal recorded by the sensor, and yield a Top-of-Atmosphere signal (Lyapustin et al., 2012). Therefore, prior to determining the relative concentrations of different OACs, an atmospheric correction is applied to correct the scattered signal and provide a clear Bottom-of-Atmosphere signal from the surface of the water (Matthews, 2011; Shanmugam, 2012). The corrected signal is known as the water-leaving reflectance ( $R_{rs}$ ) and is the ratio of the water-leaving radiance to the total downwelling irradiance from the sun recorded within each pixel of the satellite image.

Given this background, there are typically three predominant approaches to the retrieval of water quality parameters from remotely sensed imagery (Gordon & Clark, 1980). While varying in specifics, these three methods estimate water quality by establishing a relationship between the water-leaving reflectance and the concentration of different OACs. The first method is the analytical approach, whereby the way in which light is absorbed or scattered as a result of the

presence of OACs are derived from the water-leaving reflectance ( $R_{rs}$ ) and then used to quantify water quality measurements using physics modelling (eg: bio-optical and radiation transmission models) (Gilerson et al., 2010; Gons, 1999; Gordon et al., 1975; Palmer et al., 2015). However, modelling the transmission of radiation requires the in-situ measurements of many factors. Furthermore, the spectral resolutions of many satellite sensors are different than spectral resolutions of handheld sensors used near the surface of the water, which lead to complications when building the models. Therefore, although the analytical approach performs well in many aquatic environments, it is limited in its practical applicability.

The second and less complex method is the empirical approach, whereby a statistical regression is built using the relationship between ground measured “in situ” water quality measurements and the reflectance of a certain band or combination of satellite bands (Ouma et al., 2018). This method is easy to use, and its accuracy can be increased with sensors of higher spatial resolution (Li et al., 2017). Empirical approaches have been used to quantitatively derive water temperature (Brewin et al., 2018; Giardino et al., 2001; Smit et al., 2013; Vanhellemont, 2020), chlorophyll-a (phytoplankton pigments) (Gilerson et al., 2010; A. A. Gitelson et al., 2009; Kallio et al., 2001), phycocyanin (cyanobacterial pigment) (Hunter et al., 2009; Ruiz-Verdu et al., 2008), CDOM (Joshi et al., 2017; Kowalczyk et al., 2005; Kutser et al., 2005) and water clarity (Bonansea et al., 2019; Delegido et al., 2019; Petus et al., 2010). Empirical approaches can be regionally limited, thus it is often difficult to extrapolate an established model to new water bodies beyond the original sampling region.

The third approach is a semi-empirical approach, which combines analytical and empirical approaches. Unlike the empirical approach (whereby new combinations of satellite bands are formed), the semi-empirical approach relies on spectral signatures derived from previous studies to choose the band combinations. These band combinations are then used to fit a regression model to categorize the relationship with ground-verified samples (Ansper & Alikas, 2019; A. Gitelson, 1992; O'Reilly et al., 1998; Soomets et al., 2020). The semi-empirical approach retains the ease of use associated with the empirical approach yet requires a smaller sample of in-situ data and is often more regionally transferrable.

#### **1.4 Remaining Research Gaps in the Remote Sensing of Small Water Bodies**

Historically, monitoring of water quality via remote sensing has focused largely on marine ecosystems (Downing, 2014; Jerlov, 1976; Morel & Prieur, 1977; Preisendorfer, 1976). Despite its clear success, ocean colour monitoring satellites often have sensors of coarse spatial resolution (~1-5 km), ill-suited for applications in smaller inland water bodies (Chen et al., 2013; Palmer et al., 2015). Additionally, inland water bodies are optically complex, containing a wide variety of OACs, and high concentrations of phytoplankton that fluctuate throughout space and time (G. Quibell, 1992; A. Gitelson, 1993), creating more challenges for the retrieval of water quality measurements in comparison to ocean and coastal systems (R. Bukata, 2013; Palmer et al., 2015). In inland water bodies, high concentrations of mineral particles, detritus, phytoplankton biomass and CDOM can affect the absorption and scattering of light (Gordon & Morel, 1983; Morel & Prieur, 1977), and such concentrations can fluctuate and vary seasonally both among and within water bodies. In addition, the proximity of small inland water bodies to nearby land surfaces can introduce difficulties in atmospheric correction models and mixing of land and water features in pixels.

An important component of the United Nations' Sustainable Development Goals (Indicator 6.3.2) includes a focus on tracking the percentage of water bodies with acceptable water quality and inland water bodies are being increasingly recognized for their global importance to ecosystem services (Bastviken et al., 2011; de Groot et al., 2012; Jenny et al., 2020; Williamson et al., 2009). As such, many projects have been launched to monitor large inland water bodies using remotely sensed imagery. Such projects include the UK Natural Environment Research Council GloboLakes project, the Copernicus Global Land Service (CGLOPS), Global Lake Sentinel Services (GLaSS) project, and UNESCO's International Hydrological Programme (IHP). This increased funding for freshwater monitoring using remote sensing has led to the growth of research in this area (R. Bukata, 2013; Matthews, 2011; Palmer et al., 2015; H. Yang et al., 2022). Despite this growth, a research gap remains for arid/semi-arid regions where extremely small inland waterbodies (e.g.,  $< 0.01 \text{ km}^2$ ) are prevalent and quite important to human health and wellbeing. With increased access to high resolution remote sensing imagery (i.e.  $< 10\text{m}$ ), monitoring the water quality of these small water bodies may become a cost-effective way to achieve the SDG target to improve ambient water quality. Deeper exploration of the role of high spatial resolution imagery for monitoring smaller inland water bodies is a research and humanitarian imperative.

### **1.5 Research Objectives**

In this research, I developed and evaluated a new approach to remote sensing of water scarcity and water quality using high spatial resolution imagery in an arid/semi-arid region where small water bodies are critical to local livelihoods. I used a semi-empirical approach to calibrate water

quality models that were then used to estimate two key water quality parameters in small-scale water reservoirs in Narok, Kenya. I aimed to complete three main research objectives:

- I) Build a semi-empirical model to estimate water quality of small inland water bodies,
- II) Examine the regional spatio-temporal trends in water quality of small inland water bodies, and
- III) Examine the vulnerability of small water bodies to drying throughout the year.

To achieve these objectives, first, in-situ measurements of chlorophyll-a and turbidity were collected by collaborators at the Maasai Mara University. I used these field data to calibrate remotely sensed models of water quality using two high spatial resolution satellites. The best fit models were then used to extrapolate water quality measurements in reservoirs across the region and examine land-use patterns as related to water quality. Finally, I used high spatial resolution imagery to track the size and “dry up” of reservoirs over time. Together, the outcomes of these objectives were used to provide further context on the best locations to build future reservoirs.

## **Chapter 2: Methods**

### **2.1 Introduction**

East African countries are especially vulnerable to water stress and scarcity as climate in this region has changed dramatically in recent decades, impacting patterns of precipitation. Severe inter- and intra-annual variability in rainfall and temperature has now become the norm (Nicholson, 2015), making agriculture a risky endeavor for smallholder farms in arid/semi-arid regions of East Africa. Farmers in the region traditionally take advantage of the long rainy season by beginning to plant their crops in early spring. However, declining precipitation during the long rainy season has severely diminished the food security of the region (Funk et al., 2008; Lyon & DeWitt, 2012). Conversely, the short rainy season has become wetter, leading to more frequent flooding events (Liebmann et al., 2014; Nicholson, 2015).

Water-stress is particularly pronounced in the Horn of Africa, and especially Kenya. With below average rainfall and four consecutive failed rainy seasons over the 2018-2022 period, Kenya is in the middle of the worst drought experienced in the last 40 years (Office for the Coordination of Humanitarian Affairs, 2022). Worsening water quality is further reducing the amount of freshwater that can be safely used (Water Services Regulatory Board, 2022). These same areas are home to numerous nomadic pastoral livestock-keeping communities whose traditional nomadic livelihoods depend on movement to access water (and other) resources. Without clean dependable water sources for cattle during the dry season, these communities face severe impacts to their livelihoods, food security, and well-being.

To cope with prolonged periods of water-stress, the Kenyan people have built numerous small-scale reservoirs scattered throughout the country, known locally as “water-pans”. Water-pans (hereafter referred to as reservoirs) are small depressions in the landscape that act as catchments, and commonly collect water either through direct precipitation or surface runoff. These reservoirs function as sustainable, low-cost water sources for livestock, wildlife, and small-scale row-crop agriculture. Prior to construction of small-scale reservoirs, water collection was often a costly and time-consuming endeavor, with households traversing long distances daily to the nearest borehole or stream (Odiwuor, 2022). Pastoralists would trek similarly long distances, along with their entire livestock herd. Thus, monitoring the availability and status of small-scale reservoirs, and their reliability over time, are of paramount concern in parts of Kenya.

In 2018, the Kenyan government along with the World Bank launched a billion-dollar North and Northeastern Development Initiative (NEDI), a program to invest in transformative integrated infrastructure. The Kenya Climate Smart Agriculture Project (KCSAP) sits at the core of the initiative, with one aim being building climate resilient infrastructure for smallholder farmers and pastoralists including the construction of community reservoirs. The NEDI initiative only serves 10 counties in the north, with almost no programs currently in place for climate resilient infrastructure in southern counties. As a result, small-scale reservoirs in these southern regions are predominantly built by local communities, churches, and sometimes by the government alongside road construction. In Narok County, the Narok government plans to build 130 new reservoirs by 2022/2023 (County Government of Narok, 2018). However, to date, there has been little effort made to map all current reservoirs, and few studies assessing their water quality in Narok (Augustine et al., 2015). Thus, a regional examination of the past, present and future distribution

of reservoirs is vital for the Narok government planning. To support these goals in Narok, as well as support improved monitoring methods for small-scale reservoirs elsewhere, this thesis tackles three main objectives:

- I) Build a semi-empirical model to estimate the water quality of small inland water bodies,
- II) Examine the regional spatio-temporal trends in water quality of small inland water bodies, and
- III) Examine the vulnerability of small water bodies to drying throughout the year.

## **2.2 Methods**

### **2.2.1 Description of Study Region**

Narok county is a county in the southwestern portion of Kenya along the Great Rift Valley (Figure 1) with the main economic activities being tourism, pastoralism, and row crop agriculture (wheat, barley, and tea). Narok is known for its Maasai Mara Game Reserve which extends into Tanzania (known as the Serengeti National Park). The 1,510 km<sup>2</sup> reserve was established in 1961 and is one of the most important wildlife conservation areas in Africa and is the site of the Great Wildebeest migration. The reserve is named after the Maasai people, who are the ancestral inhabitants of the area along with the Kalenjin people. Together these two communities make up much of Narok's population, and practice multiple types of pastoralism. Pastoralism is the main livelihood of approximately 268 million people in Africa (FAO, 2018) and is a form of animal agriculture whereby livestock are herded onto pastures for grazing. However, the Maasai and the Kalenjin practice nomadic and semi-nomadic pastoralism, by which they herd their livestock through various regions to access natural resources throughout the seasons (FAO, 2018).

The mean annual precipitation in the region is 775 mm y<sup>-1</sup>. Precipitation in the region is characterized by two wet seasons; the first spanning March to May, and the second from September to December. The first wet season is known as the “long rains” with an average of 154 mm of precipitation in March, with April experiencing the most wet days of the entire year. The second wet season - known as the “short rains” - is characterized by sporadic and unpredictable precipitation averaging 151 mm in December. The mean annual temperature in Narok is approximately 17.8° C, with maximum temperatures in February (27 ° C) and July being the coldest month with minimum temperatures of 11.2° C. Narok contains two large perennial rivers; the Mara River and the Ewaso Narok. These rivers are the only permanent sources of water in the county, further emphasizing the need for more robust sources of water throughout the region.

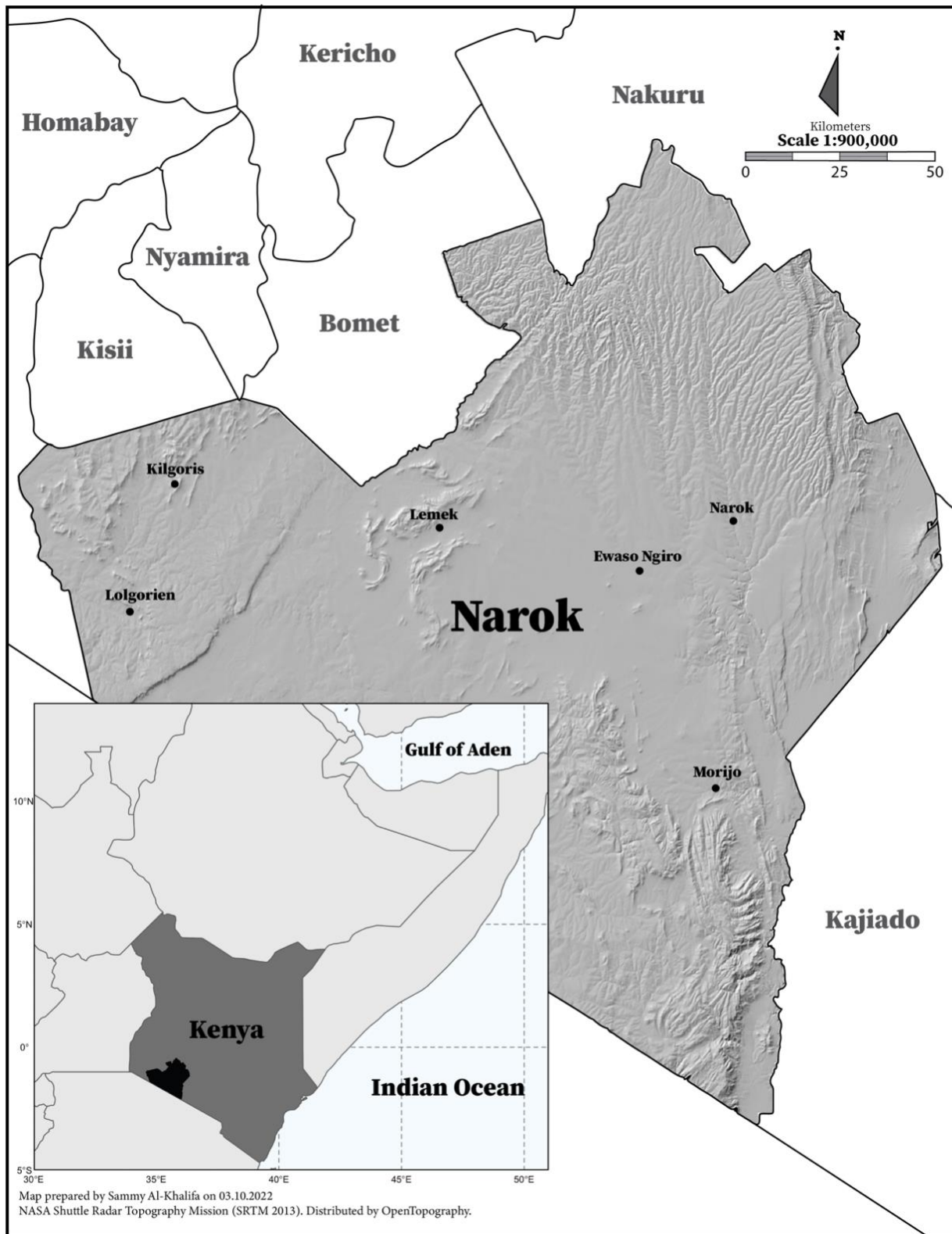


**Figure 1: Location of Narok county, Kenya, with major towns as well as neighboring counties shown. Located in the southwestern portion of the Great Rift Valley, between the latitudes  $0^{\circ} 50'$  and  $1^{\circ} 50'$  south, Narok county shares a border with Tanzania to the south. Narok county is known for the Maasai Mara National Reserve which transitions into the Serengeti National Park in Tanzania.**

### 2.2.2 Methods Overview

Within this region, I aimed to identify reservoirs situated in different land use contexts for further analysis using water quality sampling and remote sensing. To do so, three 500 km<sup>2</sup> zones were identified across Narok county capturing a land-use gradient from north to south (Figure 2).

Zone 1 is heavily comprised of agricultural landcovers, zone 3 is heavily comprised of Shrubland, and zone 2 represents a transition zone between the two zones with moderate forest cover. The cropland zone (zone 1) is the northern most zone, situated close to the Mau Forest at an average elevation of 1980 masl. The shrubland zone (zone 3) is the furthest south and is approximately 93 meters lower in elevation compared to the cropland zone. The transition zone is situated in between the other two zones at an elevation of approximately 1873 masl. Although the cropland zone is at a higher elevation, mean annual precipitation only varies by 1mm between the three zones (Funk et al., 2015). Within each zone, 10 medium-large reservoirs ranging in size from 300 – 10,000 m<sup>2</sup> were chosen. Monthly in-situ water quality measurements consisting of Chl-a and turbidity were taken for these 30 reservoirs from November 2021 to February 2022. Additional datasets included satellite imagery from both Sentinel-2 and Planet satellites, Land Cover maps (ESRI 2020), Shuttle Radar Topography Mission (SRTM) digital elevation model, road maps (OSM), and reservoir type (Figure 3). Empirical relationships were then fit between the in-situ water quality measurements (dependent variable) and the additional datasets to build water quality models (objective I). Models were then used to achieve the second objective of examining regional spatio-temporal trends in water quality. Finally, I used the PlanetScope satellite imagery to assess the vulnerability of reservoirs to drying out (objective III). Next, I explain these steps in greater detail.

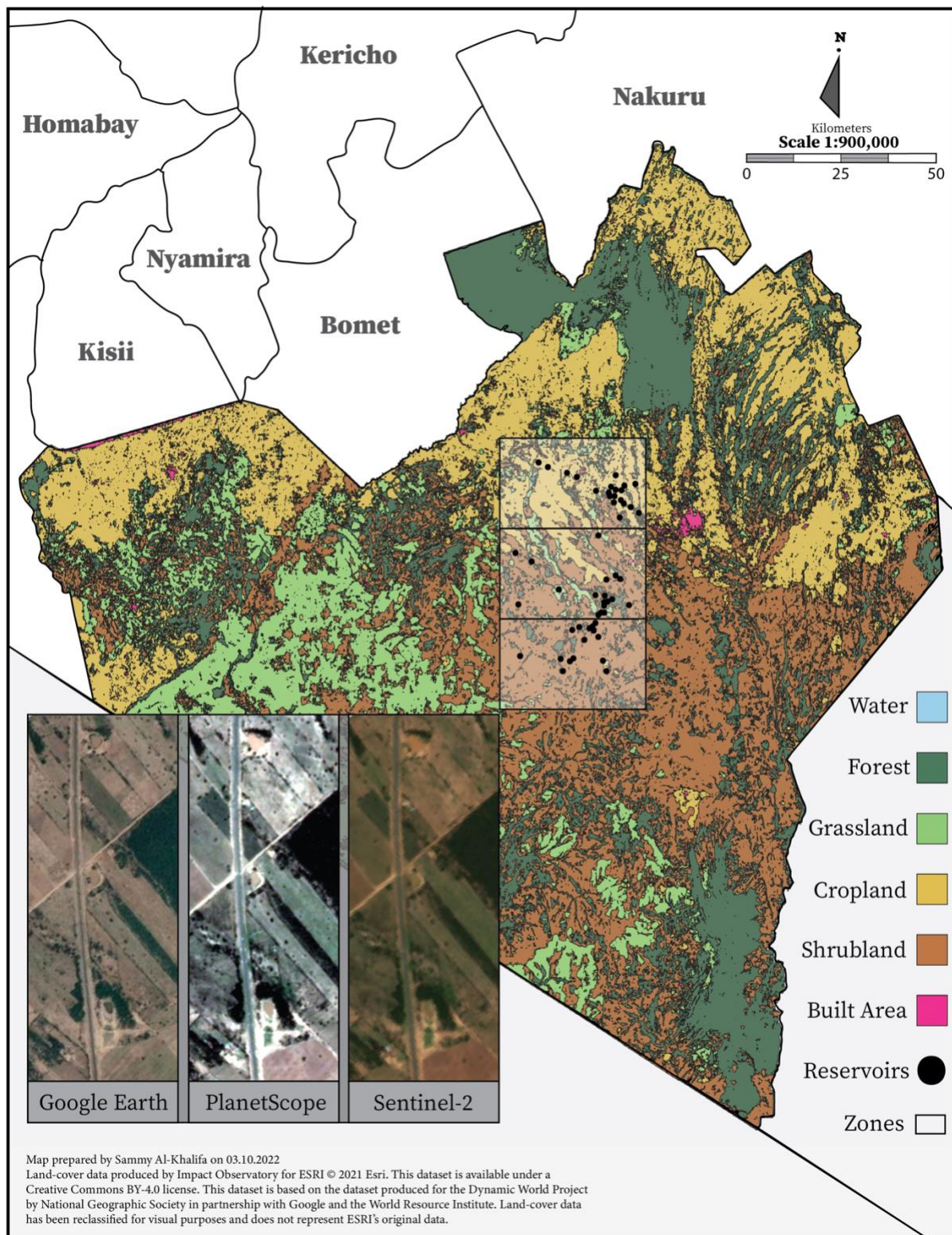


**Figure 2. Dominant land covers in Narok county, Kenya with three study zones (outlined in boxes) capturing a gradient of land-use from North to South. The northernmost zone is cropland dominated, the middle zone is a transition zone, and the southernmost zone is shrubland dominated. Panels of satellite imagery are available to visualize differences in spatial resolution between the satellite sensors used in the model building.**

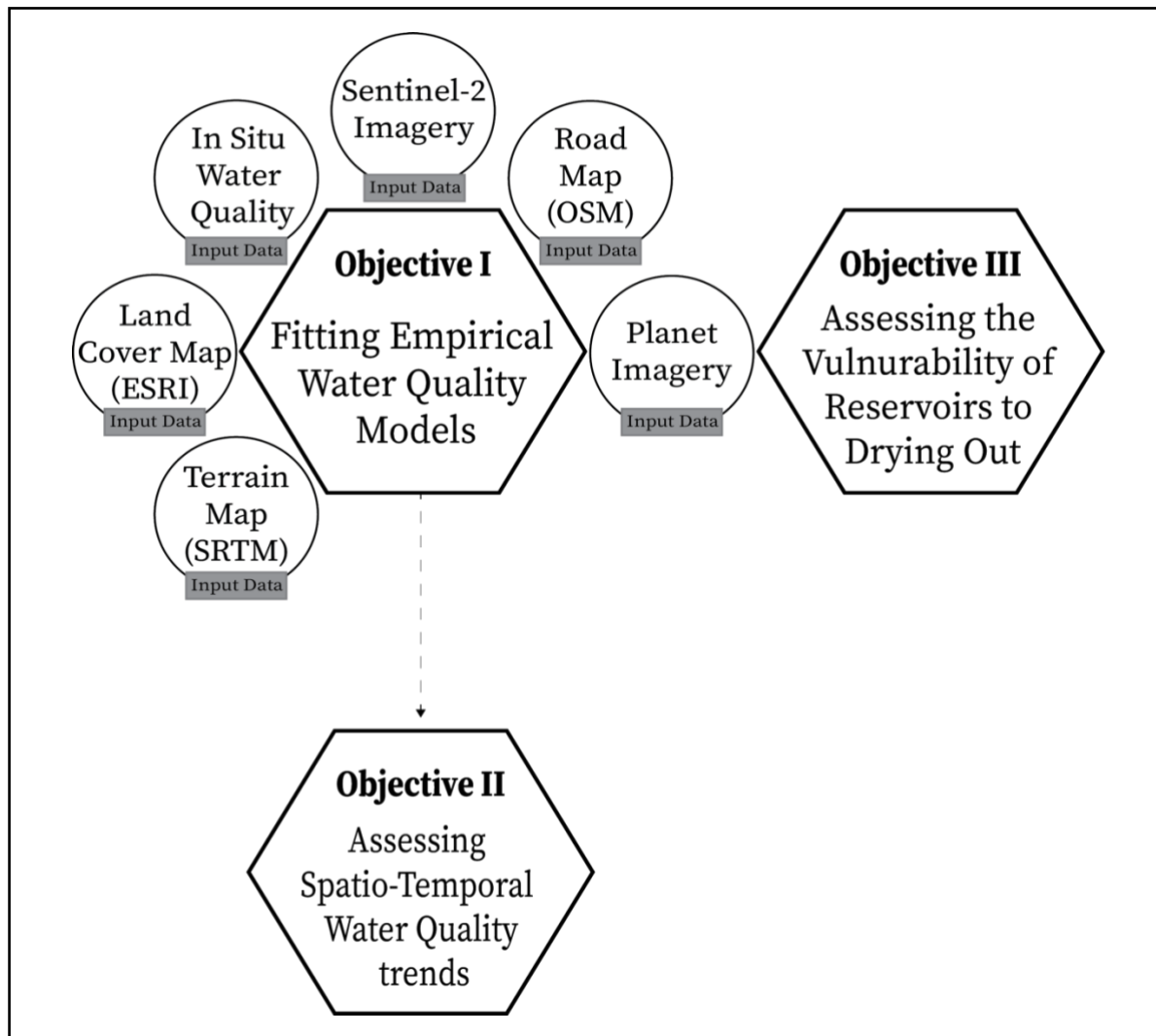


Figure 3. Input data and methods summary for three research objectives. First, an empirical relationship was established (objective 1) between in situ water quality (from 30 reservoirs) and remote sensing indices (based on PlanetScope and Sentinel-2 imagery), while accounting for land cover (ESRI global 10m map), terrain (Shuttle Radar Topography Mission Digital Elevation Map), and roads (Open Street Map). The strongest empirical models were then used to estimate the water quality of 60 reservoirs across a land-use gradient and used to achieve objective 2. Lastly, the higher resolution PlanetScope imagery (3m) was used to map and quantify the seasonal changes in areal extent in reservoirs (objective 3).

### 2.2.3 In situ Water Quality Sampling (Chlorophyll-a and Turbidity)

In situ water quality measurements were taken for a subset of reservoirs across a land-use gradient using a handheld YSI ProDSS multiparameter field sonde. Measurements of temperature (°Celsius), conductivity (uS/cm), atmospheric pressure (mmHg), turbidity in Nephelometric Turbidity Units (NTU), and chlorophyll in Relative Florescence units (RFU)

were taken for 30 reservoirs using Temperature/Conductivity, Turbidity, and Total Algae-Phycocyanin (TAL-PC) sensors. Chlorophyll is a green pigment found in photosynthesizing microalgae known as phytoplankton. These algae are not only a direct indicator of trophic status (the productivity of a water body) but are also sensitive to environmental changes such as nutrient, contaminant, and temperature fluctuations. Thus, as a useful indicator of phytoplankton biomass, chlorophyll can be used to identify water bodies which may experience toxic algal blooms throughout the year. Additionally, turbidity is a relative measure of water clarity, calculated by the amount of light that is absorbed, reflected, and scattered by water molecules. Turbidity can provide a measurement for the relative amount of sediment in water. High turbidity not only limits its use as a drinkable, potable water source, but can also have large impacts on aquatic organisms by affecting oxygenation, limiting visibility, and degrading aquatic habitats. Together, chlorophyll-a and turbidity provide specific quantitative measures of water quality by characterizing algal biomass and water clarity, respectively.

In each zone, 10 large reservoirs were sampled (at least twice) from November 2021 to February 2022 to capture rapid changes in chlorophyll and turbidity expected from the short rains to the first dry season. Additionally, four reservoirs within each of the 3 zones were selected for more rigorous repeat sampling. These 12 reservoirs were sampled monthly (near the end of each month) from November to February. In total, 84 samples (30 in Nov, 12 in Dec, 12 in Jan, 30 in Feb) were planned to be taken for chlorophyll and turbidity measurements from November to February across all three zones, however due to logistical issues with sampling only 77 samples were obtained.

To sample each reservoir, the sensors were first calibrated by the field team. The turbidity sensor was calibrated at two points, using 0 NTU and 126 NTU turbidity standards. For each point in the calibration, 170 ml of the standard was poured into a YSI calibration cup, held at a 45-degree angle to avoid bubbles in the standard. The handheld ProDSS (with the probe guard attached) was slowly dipped into the standard and held for 20 seconds or until a steady reading was reached. After confirming the first point in the calibration on the ProDSS screen, the calibration cup was emptied, rinsed, and refilled with 170ml of the second standard whereby the process was repeated. The TAL-PC sensor was also calibrated at two points, using deionized water and 800 ppb Rhodamine WT dye (diluted to 625 ppb in deionized water).

Once correctly calibrated, the sensors were attached to a 4-meter telescopic pole and dipped into the center of each reservoir to approximately 15cm in depth. The sensors were held in the water for 30 seconds, or until a stable reading was reached. Three such measurements were taken for each reservoir during each visit to ensure accurate readings. Any Chl-a or turbidity measurements that were taken before the sensor reached a stable reading were considered spoiled readings and excluded from subsequent calculations. The mean, median and maximum readings of Chl-a and turbidity for each visit was taken and used as the dependent variable in the water quality models (discussed below). Furthermore, phytoplankton migrate vertically throughout the water column throughout the day (a process known as diurnal migration) in order to maximize photosynthesis while minimizing their exposure to heat and predation. As a result, phytoplankton are often more abundant near the water surface in cooler mornings. Thus, measurements were collected between 6:00am-12:00pm.

#### **2.2.4 Satellite Imagery and Band Selection**

Imagery from Sentinel-2 and PlanetScope satellites were acquired once per month, coinciding with days of in situ sampling ( $\pm 4$  days) to aid the building of robust empirical relationships. Sentinel-2 is a high-spatial resolution (10m) land monitoring mission of the European Space Agency's Copernicus Programme (Sentinel User Handbook and Exploitation Tools, 2015). The mission is comprised of twin polar-orbiting satellites and collects imagery useful for water quality assessment due to its high spatial resolution and relatively quick return period ( $\sim 5$  days). Additionally, all Sentinel-2 products are publicly available, making Sentinel-2 one of the finest spatial resolution, open source, satellite datasets. Sentinel-2 satellites capture 13 spectral bands spanning the visible to shortwave infrared. Data acquired by the sensors is provided at L1C (Top-Of-Atmosphere) and L2A (Bottom-Of-Atmosphere) level products. In total, 43 multi-band Bottom-Of-Atmosphere Sentinel-2 products representing 3 years and 7 months (2019-2022) of consecutive images (one per month) over the entire study region were acquired using the `sen2r` library (Ranghetti et al., 2020) in RStudio.

PlanetScope imagery is created by the California-based company Planet Labs. PlanetScope is comprised of a constellation of over 200 miniature 4 kg satellites (known as Doves) launched into orbit onboard other rocket launch missions. The constellation offers daily imagery at 3-5m spatial resolution, providing fine-scale imagery on almost any day of the year. However, the imagery is not publicly available and only accessible with a licensed purchase. The onboard sensors provide imagery in 4 spectral bands from visible to near-infrared. Data acquired by the sensors is radiometrically calibrated and atmospherically corrected. In total, I gathered 43 multi-

band bottom-of-atmosphere surface reflectance Planet images representing 3 year and 7 months (2019-2022) of consecutive monthly images over the entire study region using the Planet Explorer API (Planet Team, 2022).

Together, Sentinel-2 and Planet satellites offered high spatial resolution and quick return periods suitable for monitoring the water quality of small reservoirs. While Sentinel-2 products have a higher spectral resolution (13 bands) enabling a more nuanced spectral investigation of optically active constituents OACs in water bodies, Planet imagery offers a much higher spatial and temporal resolution, which could be invaluable for retrieving water quality measurements in small, seasonally dynamic reservoirs.

To further analyze this imagery, each monthly image was cropped to the extent of the reservoir boundaries to reduce processing time in subsequent calculations. Once cropped, a series of band ratios and indices were calculated separately for both the Sentinel-2 and Planet imagery datasets (Table 1). The chosen band indices were well-established in previous studies and take advantage of the spectral properties of both algae and sediment in water. As the boundaries of reservoirs are often comprised of sand and its associated bright reflectance could confound water quality estimates at reservoir edges, I identified the centroid of each reservoir polygon using the RGEOS library in RStudio. Then, bilinear interpolation of the four pixels nearest the centroid point was used to estimate water quality for a given reservoir. In total, 21 band ratios and indices were calculated using the Sentinel-2 monthly images (14 for chlorophyll and 8 for turbidity). To further evaluate the efficacy of using the Sentinel-2 imagery for such small water bodies, this entire process was repeated using the higher spatial resolution PlanetScope imagery. However,

due to the limited number of bands available with Planet imagery, only 10 band ratios and indices were calculated (5 for chlorophyll and 5 for turbidity). A full list of all the band ratios and indices used can be found in Table 1, however a subset of the most used band ratios and indices are explained in more detail below:

The first band index is the Blue-Green algorithm, which uses the reflectance values at 490nm and 560nm respectively. The first absorption peak of chlorophyll is around 440-490nm while absorption of all photosynthetic pigments is minimal at around 550-560nm. This algorithm was first proposed for use in chlorophyll dominated oceanic waters (Morel & Prieur, 1977).

$$I) \quad chla = R(\lambda_{490})/R(\lambda_{560}) \quad [\text{Blue-Green algorithm}]$$

Algorithms that take advantage of the blue and green wavelengths excel in chlorophyll dominated waters, but can sometimes fail in waterbodies with different amounts of optically active constituents (OACs) due to backscattering and absorption from total suspended matter and coloured dissolved organic matter (CDOM). In such cases, the NIR-Red algorithm takes advantage of the second absorption peak of chlorophyll at around 665nm. Furthermore, the NIR wavelengths at ~700-720nm (Red-Edge wavelengths) are minimally absorbed by OACs (Lins et al., 2017), thus reducing complications.

$$II) \quad chla = R(\lambda_{705})/R(\lambda_{665}) \quad [\text{NIR-Red algorithm}]$$

The third band index is the Normalized Difference Chlorophyll Index (NDCI), which takes advantage of the peak reflectance of sediments at around 700-720nm (Red-Edge wavelengths) as well as the absorption peak of chlorophyll at around 665nm (red wavelengths). This makes the NDCI a powerful predictor of chlorophyll in productive waterbodies with high turbidity (Mishra & Mishra, 2012).

$$\text{III) } chla = \frac{R(\lambda_{705}) - R(\lambda_{665})}{R(\lambda_{705}) + R(\lambda_{665})} \quad [\text{NDCI}]$$

The fourth band index is the Three-Band algorithm, first developed by Dall’Olmo and Gitelson in 2005 and uses a red (665nm) and two NIR (700-740) wavelengths (Red-Edge bands in Sentinel-2) (Dall’Olmo & Gitelson, 2005). This algorithm is an accurate estimator of chlorophyll in productive water bodies with high turbidity, and was later validated by Moses (Moses, 2009). The algorithm makes some key assumptions: (1) absorption of CDOM, and total suspended matter at 700nm is equal to their absorption at 665nm, and (2) the absorption of CDOM, suspended matter and chlorophyll is approximately 0 beyond 730nm.

$$\text{IV) } chla = \left( \frac{1}{R(\lambda_{665})} - \frac{1}{R(\lambda_{705})} \right) * R(\lambda_{740}) \quad [\text{Three-Band algorithm}]$$

The Normalized Difference Turbidity Index (NDTI) takes advantage of wavelengths in the red region (~665nm) and the green region (~560nm). A water body free of any other OACs will have high reflectance in the blue (490nm) wavelengths and minimal reflectance in the green (560nm) with little to no reflectance in the red (665nm), and NIR (840nm) wavelengths. The use of these waterbodies by cattle increases the amount of sediment in the water, which reverses the relationship and leads to more reflectance in the red portion compared to the green portion (Lacaux et al., 2007).

$$\text{V) } Turbidity = \frac{R(\lambda_{665}) - R(\lambda_{560})}{R(\lambda_{665}) + R(\lambda_{560})} \quad [\text{NDTI}]$$

Lastly, the Normalized Difference Pond Index (NDPI) by Lacaux et al. (2007) was created specifically for small turbid water bodies in semi-arid regions. The logic is similar to that of the NDTI, however wavelengths around ~1600nm (Short-wave infrared band in Sentinel-2) are used as they are heavily absorbed by water.

$$\text{VI) } \textit{Turbidity} = \frac{R(\lambda_{1610}) - R(\lambda_{560})}{R(\lambda_{1610}) + R(\lambda_{560})} \quad [\text{NDPI}]$$

**Table 1. Summary of the single bands, ratios and indices investigated to estimate chlorophyll-a and turbidity using Sentinel-2 and Planet imagery. In total, 21 bands, indices, and ratios were investigated for both Chl-a and turbidity. All bands and band combinations were used as explanatory variables in a multiple regression model used to estimate turbidity and Chl-a.**

Water Quality Measure(s)	Satellite(s)	Empirical Equations	Reference
Chl-a	Sentinel-2	$R(\lambda_{443})/R(\lambda_{560})$	(Chavula et al., 2009)
Chl-a	Sentinel-2	Three Band Algorithm	(Dall’Olmo & Gitelson, 2005)
Chl-a	Sentinel-2	NDCI	(Mishra & Mishra, 2012)
Chl-a	Sentinel-2	SABI	Alawadi 2010
Chl-a	Sentinel-2	MCI	(Gower et al., 1999)
Chl-a	Sentinel-2	$R(\lambda_{705})/R(\lambda_{665})$	(Ammenberg et al., 2002)
Chl-a	Sentinel-2	$R(\lambda_{740})/R(\lambda_{665})$	(Moses, 2009)
Chl-a	Sentinel-2	$R(\lambda_{665})/R(\lambda_{560})$	(Matthews, 2011)
Chl-a	Sentinel-2	$R(\lambda_{740})$	(Bramich et al., 2021)
Chl-a	Sentinel-2/Planet	$R(\lambda_{665})$	(Jensen, 2005)
Chl-a	Sentinel-2/Planet	$R(\lambda_{490})/R(\lambda_{560})$	(Moses, 2009)
Chl-a	Sentinel-2/Planet	$R(\lambda_{560})/R(\lambda_{490})$	(Xu et al., 2022)
Chl-a	Sentinel-2/Planet	$R(\lambda_{842})/R(\lambda_{665})$	(Han & Rundquist, 1997; Moses et al., 2009)
Chl-a/Turbidity	Sentinel-2/Planet	$R(\lambda_{842})$	(Jensen, 2005)
Turbidity	Sentinel-2	NDTI	Lacaux et al. 2007
Turbidity	Sentinel-2	NDPI	Lacaux et al. 2007
Turbidity	Sentinel-2/Planet	$R(\lambda_{490})$	(Kirk, 1983)
Turbidity	Sentinel-2/Planet	$R(\lambda_{560})$	(Salem et al., 2017)
Turbidity	Sentinel-2/Planet	$R(\lambda_{665})^3$	(Mansaray et al., 2021)
Turbidity	Sentinel-2/Planet	$R(\lambda_{490})/R(\lambda_{665})$	(Jensen, 2005)
Turbidity	Sentinel-2/Planet	$R(\lambda_{560})/R(\lambda_{665})$	(Matthews, 2011)

### 2.2.5 Landscape Features

In addition to the bands, indices, and ratios explained above, features of the surrounding landscapes were also hypothesized to influence the Chl-a and turbidity in reservoirs. To account for this potential influence, five landscape features were included as explanatory variables when building the water quality models (Table 2). The proportion of each land cover class within 100 meters of each reservoir was determined. In addition, elevation (masl), distance to the nearest

road (m), and maximum size of each reservoir were also included in each model to examine the importance of these features in explaining water quality relative to the role of land cover.

In an attempt to account for the role that water volume might play in influencing water quality of reservoirs, reservoir type was used as a proxy for volume. Ground-based photos of each reservoir taken during field sampling were visually inspected to categorize reservoirs as either hand-dug or machine-excavated. Hand-dug reservoirs were generally quite shallow with gentle slopes in contrast to higher volume machine-excavated reservoirs, which were deeper and had steep slopes.

To characterize land cover within proximity of each reservoir, a 100m radius was created around each reservoir. Within each radii, percent cover of each land cover class was extracted from ESRI's 2020 global land cover map. Based on Sentinel-2 imagery at a spatial resolution of 10 meters, ESRI's classification was created using a deep learning model trained with approximately 5 billion verified Sentinel-2 pixels at over 20,000 locations globally. Their classification achieved an overall accuracy of approximately 86% on the validation set, with Croplands and Trees receiving some of the highest per-class accuracies (89% and 91% respectively). However, the map achieved relatively low accuracies for Shrublands and Grasslands (Karra et al., 2021).

**Table 2. Summary of additional explanatory variables used to fit the Chl-a and turbidity models. Variables with skewed distributions were transformed. Reservoir type refers to whether a reservoir was hand dug or machine excavated. For more information on the datasets used, see Figure 3.**

Explanatory Variable		Transformation
Proximity to Main Road (m)		Cube Root
Elevation (masl)		-
Maximum Reservoir Size (m <sup>2</sup> )		Cube Root
Reservoir Type		-
Land cover within 100m of reservoir (%)	Shrubland	Square
	Bare Ground	-
	Built Area	Log10
	Cropland	Square
	Grassland	Log10
	Forest	Log10
	Water	Log10

### 2.2.6 Statistical Analyses (Model Building and Comparison)

To achieve objective I, multiple linear regression was used to establish and evaluate the strength of empirical relationships between in situ water quality (Chl-a and Turbidity) and corresponding band combinations from Sentinel-2 and PlanetScope imagery (Table 1) plus five landscape features (Table 2). I evaluated four response variables, as follows. First, I examined both the mean and the maximum values of Chl-a using all data from all sampling months (hereafter referred to as “global models”). Second, I examined distinct sub-models for the month of February (built using only in-situ measurements and satellite imagery from February). February models were useful to examine because February was the month of greatest overall precipitation and thus was the only month with a complete set of water samples from all reservoirs. In other words, during the drier months of November and December, multiple reservoirs were completely dry and unsampled. Finally, models with each of these four response variables (global max, global mean, Feb max and Feb mean) were run twice to compare models using Sentinel-2 versus models using PlanetScope imagery, for a total of 8 models. Lastly, this entire process was repeated for turbidity (another 8 models), for a total of 16 models.

To identify the final models for each unique dependent variable, I used forward step-wise selection. To do so, a null model was fit containing no variables, and with each additional variable, AIC,  $R^2$ , and adjusted  $R^2$  values were recorded, until reaching a full model containing all variables. For a given dependent variable, all significant nested models ( $p$ -value  $< 0.05$ ) were ranked based on AIC scores and the model with the lowest AIC score was chosen as the “final” model. To ensure no multicollinearity between variables, no variable with a Value Inflation Factor (VIF) higher than 10 was included in the final model.

After determining the final model for each response variable, I further identified a “top” model used for future extrapolations as part of Objective 2. From the list of 8 final Chl-a models, I chose the top models with the highest adjusted  $R^2$  values. The process was repeated for Turbidity. Linearity and homoscedasticity were checked using residual plots. Normality of the residuals was checked using Quantile-Quantile plots, with some variables transformed where appropriate. In cases where the dependent variables needed transformation, the model extrapolations were back transformed.

### **2.2.7 Spatio-Temporal Impacts of Land-use on Water Quality**

To achieve the second objective, I used the best performing February model from objective I to estimate and extrapolate water quality (Chl-a and turbidity) for 60 reservoirs across a land-use gradient. The February sub-models (for both Chl-a and turbidity) had higher adjusted  $R^2$  values than the global models and were therefore selected to examine the spatial patterns of water quality with respect to land-use. To test for differences in estimated water quality across the three

land-use zones, a one-way Analysis of Variance was conducted followed by a pairwise T-test in R (R Core Team, 2022). Assumptions of normality and equal variance were tested using Quantile-Quantile and residual plots.

Similarly, the top global models from objective I were used to derive Chl-a and turbidity estimates for 60 reservoirs throughout the region on a monthly basis from January 2019 to July 2022, creating a time-series of 43 monthly Chl-a and turbidity estimates for each reservoir. Global models were used for timeseries analyses because the models were fit using all four months of in-situ data. A nonparametric Mann-Kendall test (Kendall, 1975; Mann, 1945; McLeod, 2022) was then used to test for significant monotonic trends in Chl-a and turbidity for each reservoir. Mann-Kendall (M-K) trend tests do not allow missing values. Therefore, values for missing months (due to cloud cover or poor image quality) were interpolated using Friedman's nonparametric regression estimator (Friedman, 1984) based on local linear regression.

Theil-Sen slopes (TS) were used to quantify the relative magnitude of significant trends (Pohlert, 2020). In other words, a TS value for a given reservoir represents the median amount of change in Chl-a or turbidity per month. Reservoirs with the top 10% of TS values were distinguished as experiencing a high magnitude of change. Due to the potential for seasonal fluctuations in water quality, seasonal Mann-Kendall trend tests were conducted to identify trends in water quality after cyclical fluctuations in Chl-a and turbidity were accounted for (Hirsch et al., 1982; Marchetto, 2021). The timeseries were grouped into three seasons, defined by the long rains (March-May), the short rains (September-December), and all other months considered part of the

dry season. Similar to the Theil-Sen slopes, a seasonal Kendall slope estimator was calculated to quantify the relative magnitude of significant trends.

### **2.2.9 Tracking Seasonal Shifts in Reservoir Size**

To achieve objective 3 and determine whether reservoirs were vulnerable to drying out (in terms of reductions in surface area), I mapped areal changes in reservoir size between the wet and dry seasons in 2021. Leveraging its extremely high spatial resolution, PlanetScope imagery was used to manually digitize 60 reservoirs once during the peak dry season (Dec 2021) and again during the peak wet season (June) using QGIS software (Hannover version 3.16) in the UTM Zone 36S projected coordinate system (EPSG:32736). The digitized polygons were then imported into RStudio (2021.09.02 Build 382) where the size of each reservoir polygon was calculated in m<sup>2</sup>. The percent change was further calculated to determine which reservoirs lost more than 50% of their surface area between the two seasons. Reservoirs which surpassed this 50% threshold were considered “vulnerable” to drying out. I further used a one-way Analysis of Variance and subsequent pairwise T-test to test for differences in areal loss (in absolute and proportional terms) across the land-use gradient, to identify characteristics of most vulnerable reservoirs. The proportional change in area for reservoirs was nonnormal based on a Quantile-Quantile plot, and therefore a log base 10 transformation was used to normalize the values.

## **2.3 Results**

### **2.3.1 In-situ Samples**

Water quality in ten reservoirs across three zones (for a total of 30 reservoirs) was sampled from November 2021 to February 2022 (Table 3). Chl-a ranged from 0 -186 RFU across the entire study period with a median of approximately 7.5 RFU. Chl-a peaked in December at 26.3 RFU and gradually fell to 14.5 RFU in February. In-situ measurements of turbidity ranged from 0.7 to ~2500 NTU with a median of 357 NTU. Across all reservoirs, turbidity behaved similarly to Chl-a, peaking in December (702.8 NTU) before falling to 258.6 NTU in February.

**Table 3. Summary of in situ chlorophyll-a (in Relative Fluorescence Units) and Turbidity (in Nephelometric Turbidity Units) for 30 reservoirs sampled across 3 broad land-use zones in Narok, Kenya. Samples were taken from November 2021 to February 2022. A summary of the mean, median, maximum, and minimum values of chlorophyll-a and turbidity for each reservoir across all months were calculated and included below.**

Reservoir ID	Zone	# Dates Sampled	Chlorophyll-a (RFU)				Turbidity (NTU)			
			Mean	Median	Max	Min	Mean	Median	Max	Min
100	Cropland	2	8.6	10.9	11.7	0.7	68.9	90.1	93.5	1.9
101	Cropland	4	11.3	12.6	14.1	5.6	95.2	95.1	101.1	89.8
103	Cropland	2	9.3	9.5	18.2	0.7	276.3	339.6	446.6	2.6
104	Cropland	2	86.6	85.2	186.0	0.7	140.9	108.2	329.9	0.7
105	Cropland	2	15.0	13.8	24.6	7.9	220.8	189.1	317.2	187.6
109	Cropland	4	6.8	4.3	12.3	3.9	313.3	114.7	710.6	114.5
110	Cropland	4	75.9	125.3	160.0	0.8	702.5	364.3	2589.0	31.3
111	Cropland	2	9.3	8.0	12.3	7.7	141.0	140.7	141.8	140.5
112	Cropland	4	6.4	6.7	8.4	0.7	518.2	572.1	663.5	7.2
116	Cropland	2	14.6	15.1	19.1	9.2	303.7	259.5	441.2	254.6
221	Transition	4	9.2	6.9	43.6	4.9	741.4	710.3	862.1	439.0
222	Transition	4	38.0	38.6	75.9	4.0	660.0	665.3	872.5	180.4
223	Transition	4	3.5	4.1	5.2	0.7	133.3	176.1	177.9	3.0
224	Transition	2	10.6	12.4	13.0	4.7	527.0	711.8	763.0	9.6
225	Transition	4	6.7	7.1	12.0	0	916.6	1042.1	1431.8	2.2
229	Transition	2	5.3	5.6	6.7	2.7	708.5	744.4	1196.4	3.2
235	Transition	2	17.3	5.5	52.6	5.4	334.4	262.3	553.0	260.0
237	Transition	2	6.9	6.3	11.1	4.2	622.1	552.9	1414.9	58.8
241	Transition	2	7.0	7.9	10.8	1.2	476.8	446.3	872.5	263.6
243	Transition	2	119.5	125.4	179.0	0.7	33.5	34.7	45.3	10.5
345	Shrubland	4	9.2	7.0	33.3	0.7	149.3	134.3	382.8	4.3
348	Shrubland	4	9.2	10.4	15.7	0.4	599.9	534.0	1346.3	2.8
352	Shrubland	2	18.1	6.6	47.4	0.7	250.4	57.4	1104.6	8.9
355	Shrubland	2	6.4	6.2	7.4	5.3	689.8	718.3	1074.3	134.8
356	Shrubland	2	9.6	6.8	19.7	0.4	498.1	210.7	1069.1	2.2
357	Shrubland	2	5.0	4.8	6.4	4.3	200.7	145.3	325.2	133.6
364	Shrubland	4	14.8	12.0	28.8	0.7	568.3	450.3	1042.9	2.0
368	Shrubland	2	6.7	8.7	9.1	3.5	833.8	1285.2	1292.4	150.0
375	Shrubland	2	5.4	6.4	6.6	0.7	342.5	365.7	484.4	2.2
391	Shrubland	4	6.2	6.7	9.7	0.8	353.4	379.1	534.7	1.9

### 2.3.2 Empirical Water Quality Models

To address our first objective of building empirical relationships using remote sensing and landscape features capable of estimating water quality, I used in-situ measurements of Chl-a and turbidity from 30 reservoirs. All models were statistically significant using an alpha of 0.05. I

evaluated 8 February models and 8 global models (16 models in total) after a forward step-wise selection of variables (Table 4).

**Table 4. Summary of regression results explaining in-situ water quality as a function of remote sensing indices from two high spatial resolution sensors as well as other landscape variables (described in Figure 3). February sub-models (ie in-situ measurements and satellite imagery taken during February) were contrasted to global models fit using in situ samples and satellite imagery for all months (Nov 2021 – Feb 2022). Each model (row) was chosen after a forward step-wise selection of variables based on significance ( $p < 0.05$ ) and AIC score (lowest). Variables with VIF scores higher than 10 were excluded from the final models. February and global models with the highest adjusted  $R^2$  values (highlighted in grey below) were chosen and used for extrapolation of chlorophyll-a and turbidity to a larger set of 60 reservoirs in the region and are explained in further detail in Table 5. The sample size refers to the number of reservoirs that were sampled in-situ and used to fit the model. For a more detailed version of this table (including AIC and VIF scores), please see Appendix.**

Water Quality Measure	Sample Size	Month	Satellite	$R^2$	Adj. $R^2$	P-Value
<b>Chlorophyll-a (RFU)</b>						
max	30	February	Sentinel-2	0.69	0.64	4.2E-06
mean	30	February	PlanetScope	0.67	0.61	3.1E-05
max	30	February	PlanetScope	0.71	0.60	2.9E-04
mean	30	February	Sentinel-2	0.58	0.56	1.1E-06
max	77	all	Sentinel-2	0.54	0.50	1.0E-09
mean	77	all	Sentinel-2	0.52	0.49	9.2E-11
max	77	all	PlanetScope	0.46	0.39	8.3E-07
mean	77	all	PlanetScope	0.44	0.36	6.1E-06
<b>Turbidity (NTU)</b>						
mean	30	February	PlanetScope	0.72	0.63	7.2E-05
max	30	February	PlanetScope	0.59	0.51	3.9E-04
mean	30	February	Sentinel-2	0.68	0.60	8.6E-05
max	30	February	Sentinel-2	0.60	0.50	8.5E-04
mean	77	all	PlanetScope	0.66	0.63	4.2E-14
max	77	all	PlanetScope	0.56	0.53	4.3E-12
mean	77	all	Sentinel-2	0.49	0.47	4.2E-10
max	77	all	Sentinel-2	0.46	0.44	9.3E-10

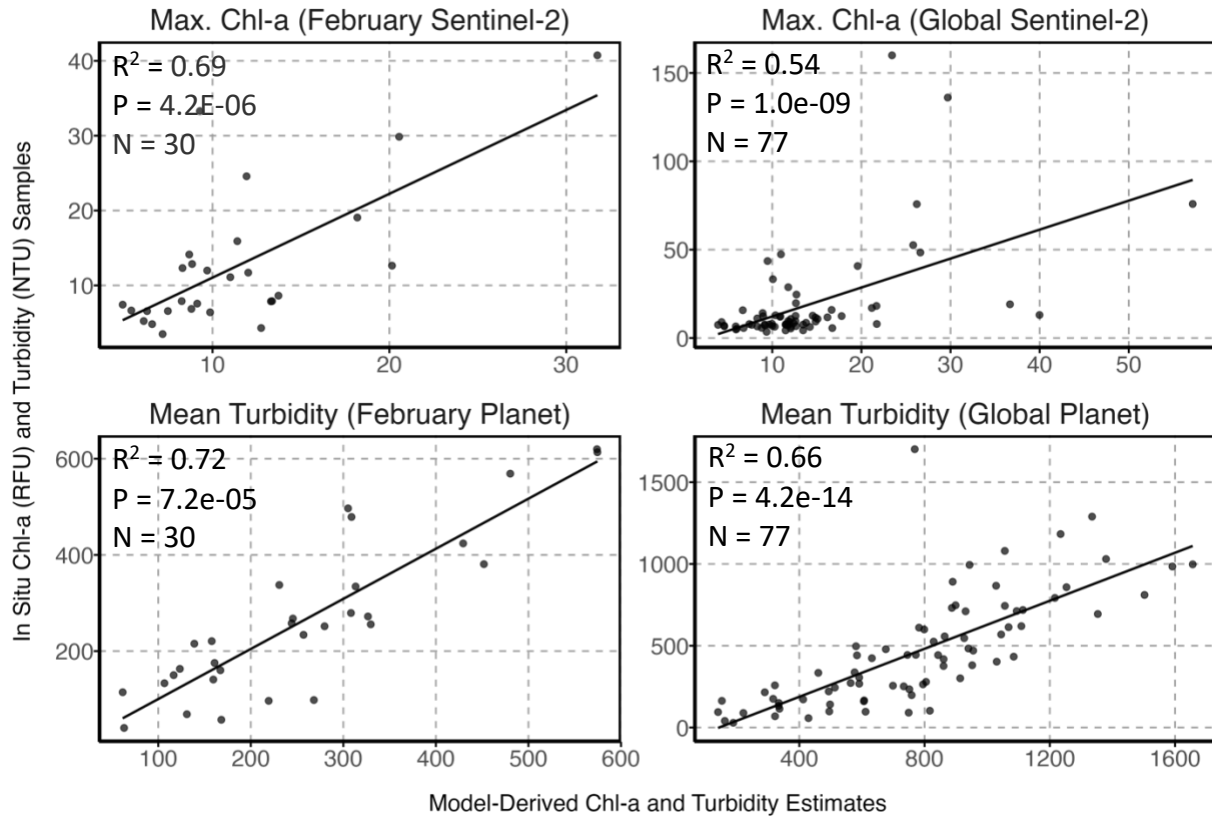
From these models, I identified the top global and February models for both Chl-a and turbidity, for a total of four top models (Table 4 and Figure 4). Throughout all models, February sub-models (fit using a single month of in situ samples and satellite imagery) had higher  $R^2$  and adjusted  $R^2$  values compared to global models (fit using in situ samples and satellite imagery for all months). Therefore, February models (for both Chl-a and turbidity) were used in a space-

based analysis to examine water quality across a land-use gradient, whereas global models were used to examine temporal trends in water quality from 2019 to 2022.

Across all Chl-a models, the variation in maximum Chl-a was better explained by the independent variables than mean Chl-a. Furthermore, the top February Chl-a model using Sentinel-2 satellites explained slightly more variation ( $R^2 = 0.69$ ) than the February model using Planet satellites ( $R^2 = 0.67$ ). Similarly, the top global Chl-a model using Sentinel-2 satellites explained more variation ( $R^2 = 0.54$ ) than the global model using Planet satellites ( $R^2 = 0.46$ ).

Across all turbidity models, the variation in mean turbidity was better explained by the independent variables than maximum turbidity. Furthermore, the top February turbidity model using PlanetScope imagery explained more variation ( $R^2 = 0.72$ ) than the February model using Sentinel-2 imagery ( $R^2 = 0.68$ ) (Table 4). Similarly, the top global turbidity model using PlanetScope imagery explained more variation ( $R^2 = 0.66$ ) than the global model using Sentinel-2 imagery ( $R^2 = 0.49$ ). Overall, Sentinel-2 imagery was deemed a better fit in estimating Maximum Chl-a for both the February and global models with  $R^2$  values 0.69 and 0.54 respectively (Table 4). Conversely, PlanetScope imagery was deemed better fit in estimating turbidity for both the February and global models ( $R^2 = 0.72$  and 0.66 respectively).

**Figure 4. Relationships between in-situ water quality (chlorophyll-a and turbidity) measurements and model-derived estimates of chlorophyll-a and turbidity (using four top models from Table 5). Model-derived estimates are based on satellite imagery from Sentinel-2 and Planetscope corresponding to the day of in situ sampling (+/- 4 days).**



The top 4 models included multiple significant remote sensing band ratios and indices. The ratios of Aerosol to Green bands were significant in both Chl-a models (based on Sentinel-2 imagery) and were negatively associated with maximum Chl-a. Additionally, the Red-Edge to Red ratio was significant in the February Chl-a model (Table 5) and was positively associated with maximum Chl-a. Additional remote sensing variables deemed significant in global Chl-a models were the ratios of NIR to Red, Red to Green, Green to Blue, as well as the Normalized Difference Chlorophyll Index (NDCI). The ratio of Green to Blue and NIR to Red were both negatively associated with maximum Chl-a, where the Normalized Difference Chlorophyll Index (NDCI) and the ratio of Red to green were both positively associated with maximum Chl-a.

Furthermore, the NIR and Red bands were used in all significant band ratios in both the top turbidity models (based on PlanetScope imagery). Specifically, bands and band ratios found to be significant in both turbidity models were Red, NIR, Blue to Red and NIR to Red (Table 5) and were all positively associated with mean turbidity. Relationships between all explanatory and response variables can be found in the appendix.

### **2.3.3 Landscape Features That Aided Water Quality Estimations**

February models (for both Chl-a and turbidity) were stronger than the global models, and the addition of landscape features in these models increased  $R^2$  values by 4 to 9% as compared to models using remote sensing variables alone. Relevant features included percent landcover, specifically the proportion of forests, grasslands, and water within 100m of each reservoir (Table 5). The proportion of grasslands and forests within 100m of reservoirs was negatively associated with maximum Chl-a in the February model (Table 5). Conversely, the proportion of forests, and water were all positively associated with mean turbidity in both the February models (Appendix A.2). Other features of the landscape such as the proximity of reservoirs to roads, and the maximum size of reservoirs were also significant in Chl-a and turbidity models (Table 5). The maximum size of reservoirs was positively associated with mean turbidity in the February turbidity model. Additionally, proximity to roads was negatively associated with mean turbidity in the February models.

**Table 5. Detailed description of the four top models (derived from Table 4) used for extrapolation of chlorophyll-a and turbidity to a larger set of reservoirs in the region. Month-specific Chl-a and turbidity models were fit using measurements taken during a single month (hence N = 30 reservoirs) whereas global models were fit using data from all months (Nov 2021 – Feb 2022) (hence N = 77). Model selection used forward step-wise selection of variables using the lowest Akaike Information Score (AIC) and Value Inflation Factors (VIF) scores less than 10. Please see Tables 1 and 2 for a list of all model variables, and Appendix A.1/A.2 for the full list of models and variables.**

Water Quality Measure	Max. Chl-a	Max. Chl-a	Mean Turbidity	Mean Turbidity
<b>Time frame of model</b>	February	Global	February	Global
<b>Satellite</b>	Sentinel-2	Sentinel-2	PlanetScope	PlanetScope
<b>N</b>	30	77	30	77
<b>Independent Variables</b>	RedEdge/Red (3.69)	log(NDCI) (17.3)	Red (0.005)	Red (0.02)
	Aerosol/Green (-0.83)	Aerosol/Green (-0.53)	NIR (0.005)	log(NIR/Red) (29.85)
	log(%Forest) (-0.08)	Red/Green (0.18)	Blue/Red (18.89)	$\sqrt{\% \text{ Shrubland}}$ (-0.0004)
	log(% Grassland) (-0.09)	Green/Blue (-1.14)	log(%Forest) (2.66)	log(%Forest) (1.46)
		NIR/Red (-0.25)	$\sqrt[3]{\text{Proximity to Roads}}$ (-0.60)	$\sqrt[3]{\text{Proximity to Roads}}$ (-0.53)
		log(%Built Area) (0.38)	$\sqrt[3]{\text{Max. Reservoir Size}}$ (0.44)	log(%Built Area) (-6.30)
		$\sqrt[3]{\text{Max. Reservoir Size}}$ (-0.01)	log(% Water) (8.69)	% Bare Ground (1.62)

However, landscape features explained less variation in comparison to remote sensing variables (Figure 5). For example, in the February Chl-a model, the amount of forest and grassland surrounding a reservoir explained less than 10% of the variation in the model. Remote sensing variables such as the ratio of Aerosol to Green and Red-Edge to Red explained approximately 18% and over 63% of the variation in the February Chl-a model respectively (Figure 5).

Conversely, the amount of forest cover surrounding reservoirs explained roughly 30% of the variation in the February turbidity model, whereas other landscape features such as the proximity of a reservoir to a road and the maximum size of the reservoir explained ~21% and ~13% of the variation respectively. Within the same model, remote sensing variables such as the Red band

and the ratio of Blue to Red explained ~26% and 12% respectively. Notably, the NIR band alone explained more than 30% of the variation in the February turbidity model.

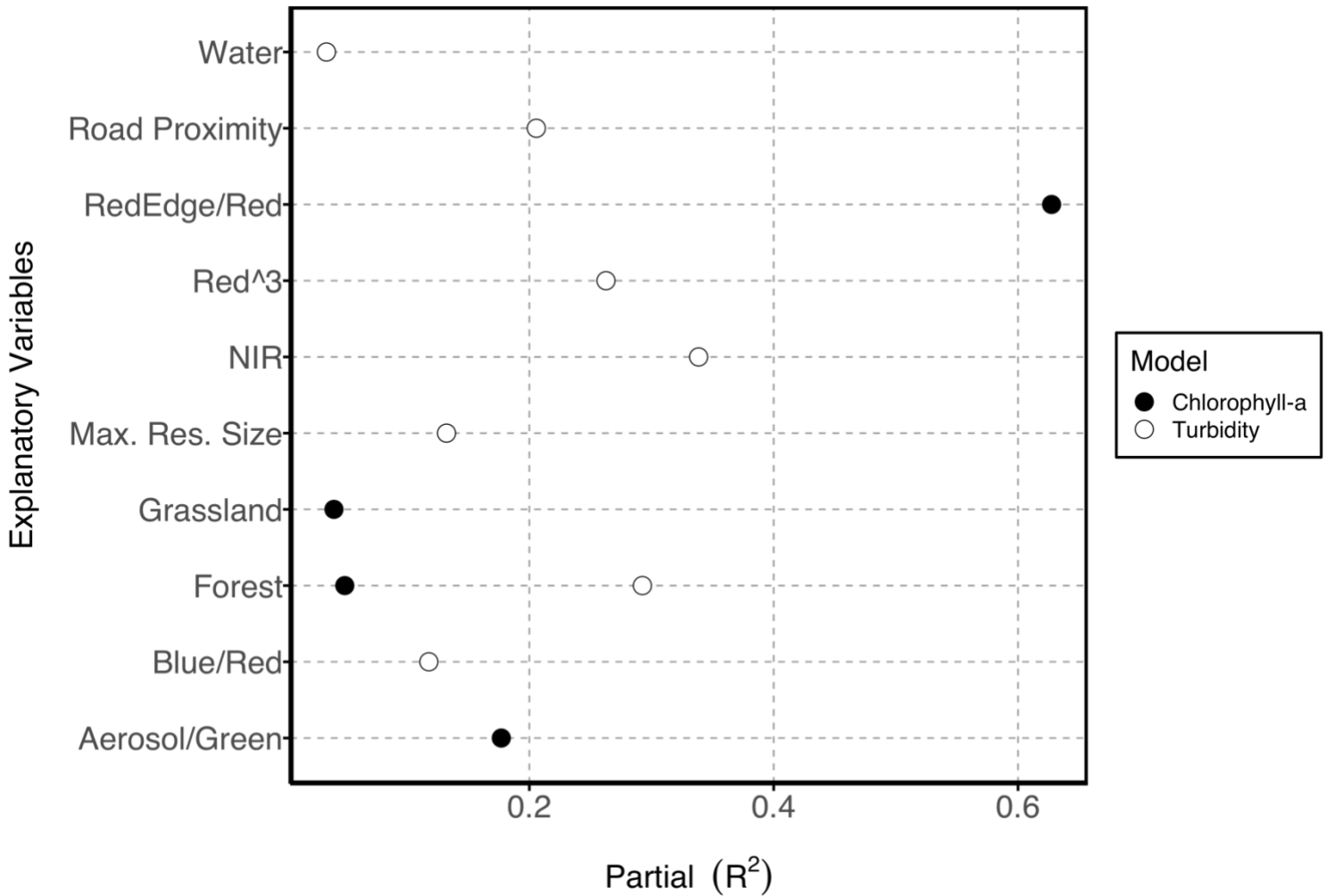


**Figure 5. Partial R<sup>2</sup> values for significant explanatory variables from the top February models for Chl-a and turbidity (Table 5). Explanatory variables included: percent landcover within 100m, elevation, maximum reservoir size, proximity to roads, and four remote sensing band indices (for a list of all explanatory variables and their transformations see Tables 1 and 2). A forward stepwise selection of variables was used to choose variables based on the lowest AIC scores and Value Inflation Factors below 10. The top February models were then used to estimate Chl-a using Sentinel-2 imagery (in black) and turbidity using PlanetScope imagery (in white) in 60 reservoirs.**

### 2.3.4 Spatio-Temporal Trends in Regional Water Quality

Due to the strength of the relationships in the February Models, these models were used in a space-based analysis to examine water quality across a land-use gradients. February models

(Figure 4) were first used to extrapolate Chl-a and turbidity to 60 reservoirs during a single month (February), and then used to examine water quality across a land-use gradient.

Median Chl-a was 11.7 RFU in the cropland dominant zone, 10.3 RFU in the transition zone and only 9.6 RFU in the shrubland zone (Figure 6). However, I found no significant differences in mean Chl-a across the three zones when using a One-Way analysis of Variance. Conversely, median turbidity was 305 NTU in the transition zone, 200 NTU in the shrubland zone, and 197 NTU in the cropland zone. I used a One-Way Analysis of Variance and found marginally significant differences in turbidity between the three zones ( $p = 0.08$ ), with the highest values being in the transition zone.

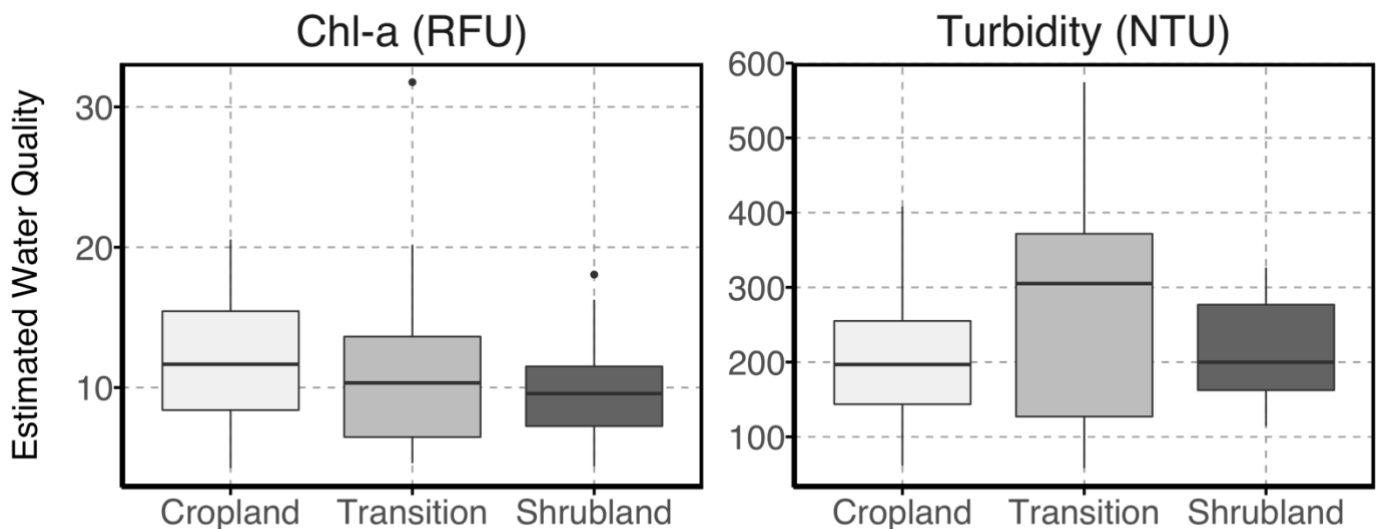


**Figure 6. Patterns of chlorophyll-a and turbidity estimated using remote sensing for 60 reservoirs across a land-use gradient from Zone 1 (agriculture) to Zone 2 (transitional) to Zone 3 (shrublands with little to no agriculture). Land cover was derived using ESRI's 2020 Global Land Cover Map at 10m spatial resolution.**

Global models (Figure 4) were then used to make Chl-a and turbidity estimations for 60 reservoirs across 43 months (January 2019 – July 2022) to examine temporal trends in water quality. Overall, significant trends in water quality were found in 49 of the 60 reservoirs from

January 2019 to July 2022. Specifically, 28 reservoirs (47%) displayed significant declining Chl-a trends ( $p < 0.05$ ) (Figure 7 & Appendix A.3d). Of these 28 reservoirs, Chl-a declined by up to 96%, with Theil-Sen slopes ranging from -0.01 to -1.1. When examining temporal trends in turbidity, half of all reservoirs examined (30) displayed significant trends ( $p < 0.05$ ) (Figure 7). Of the 30 reservoirs with significant trends, turbidity declined by up to 90% in 24 reservoirs, with Theil-Sen slopes ranging from -1.4 to -28. Additionally, turbidity increased in 6 reservoirs by up to 56% over the study period (TS ranging from 3.3 to 8.0).

I found a significant difference in the magnitude of change in Chl-a across the land-use gradient ( $p = 0.03$ ). Chl-a concentrations were decreasing most rapidly in the cropland zone ( $p = 0.02$  using a pairwise T-Test with a Bonferroni adjustment for multiple comparisons). Conversely, no significant differences in turbidity Sen slopes were found across the land-use gradient ( $p = 0.4$ ).

To examine water quality trends in reservoirs after accounting for cyclical seasonal fluctuations, I further used seasonal Mann-Kendall tests. After accounting for seasonality, significant trends in water quality (Chl-a and turbidity) were found for 42 reservoirs, two of which were new (i.e., not identified as significant in previous non-seasonal M-K tests) (Appendix A.3). I found declining Chl-a concentrations ( $p < 0.05$ ) in 24 reservoirs where Seasonal Kendall Slope estimators ranged from -1.2 to -15.7 (steeper slopes than those from non-seasonal MK tests) (Appendix A.4). Similar to non-seasonal M-K test results, I found differences in the magnitude of change in Chl-a (as measured by seasonal Kendall slopes) across the land-use gradient. Chl-a concentrations declined most gradually in the shrubland zone (mean slope = -1.9,  $p = 0.04$ ) when compared to the transition zone (mean slope = -6.1) and the cropland zone

(mean = -6.3). Furthermore, after accounting for seasonal fluctuations, I found significant trends in turbidity ( $p < 0.05$ ) in 27 reservoirs. Of these, 19 showed declining turbidity with Kendall slopes ranging from -36.1 to -313.7, steeper than non-seasonal M-K tests. A total of 8 reservoirs displayed increasing turbidity with steeper slopes than non-seasonal M-K tests (seasonal slopes ranging from 21.9 to 87.9).

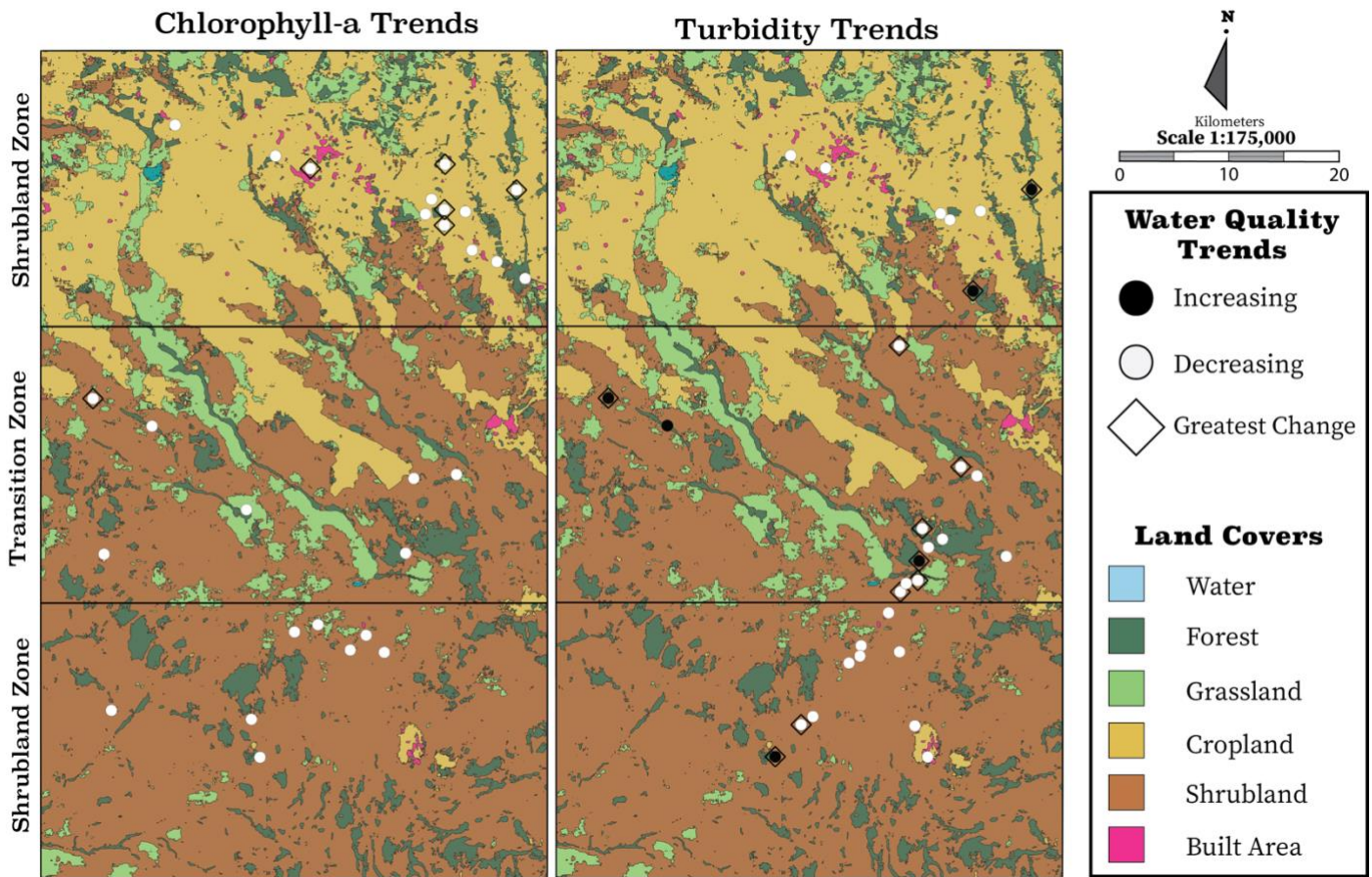


**Figure 7.** Water quality trends for 60 small-scale reservoirs across a land-use gradient in Narok, Kenya from January 2019 to July 2022. A nonparametric Mann-Kendall test was used to test for monotonic trends in Chl-a and turbidity for each reservoir. Any reservoir with significant increasing (black dots) and decreasing (white dots) trends in water quality ( $p < 0.05$ ) were further tested using a Sen’s slope estimator to determine where water quality was changing most rapidly (diamonds). The highest magnitude of change was calculated as the top 20% of Sen Slopes.

### 2.3.5 Tracking Seasonal Shifts in Reservoir Size

To detect the intra-annual changing size of reservoirs, I compared the boundaries of 60 reservoirs during the peak wet season (Jun) and the peak dry season (Dec). During the wet season, the smallest reservoir was 300m<sup>2</sup>, whereas the largest was approximately 10,000 m<sup>2</sup>. Reservoirs expanded during the long rains in June (mean = 2,609 m<sup>2</sup>) compared to the dry season in December (mean = 1,434 m<sup>2</sup>). Of all 60 reservoirs, approximately 25% completely dried out during the dry season, and 46% lost more than 50% of their surface area. The change in reservoir size amongst the three land-use zones was statistically significantly different (One-Way Analysis of Variance  $p = 0.025$ ). Reservoirs in the cropland zone lost the most surface area between the wet season and the dry season ( $p = 0.024$ ).

#### Change in Reservoir Area Across Each Zone

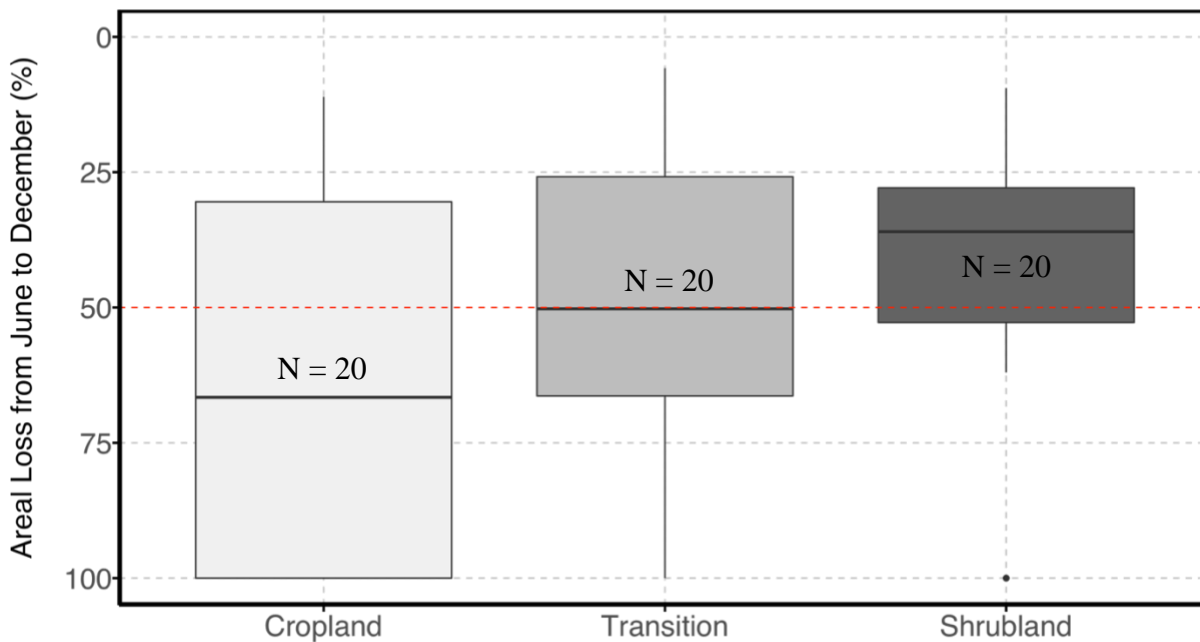


**Figure 8.** Change in reservoir size across a gradient of agricultural land use. Areal change was mapped using ~3m resolution Planetscope imagery from the peak of the wet season (June 2021) to the peak of the dry season (Dec 2021). Boundaries were delineated by manual digitization of 60 reservoirs using QGIS software (Hannover version 3.16). Zone 1 is the northern most zone and is dominated by agricultural land covers. Zone 2 is a transition zone containing Agricultural land covers, Shrublands and Forests. Zone 3 is Shrubland dominated with little to no Agricultural land covers.

## Chapter 3: Discussion

### 3.1 Key Findings

I employed a novel approach in combining remote sensing indices with landscape features which proved to be successful in modelling key water quality constituents (Chlorophyll-a and turbidity) of small-scale reservoirs. Overall, the increased spectral resolution (12 narrow bands) of the Sentinel-2 sensors produced stronger models of Chlorophyll-a ( $R^2 = 0.69$ ) whereas the high spatial resolution (~3m) and wider bands of the PlanetScope satellite was more powerful for turbidity ( $R^2 = 0.72$ ). Furthermore, introducing landscape features such as land cover, maximum reservoir size, and proximity to roads improved the power of models by roughly 4 to 9%, enabling extrapolation of water quality for 60 reservoirs over 43 consecutive months (January 2019-July 2022) across a land-use gradient.

Although I found no significant differences in Chlorophyll-a (Chl-a) across the land-use gradient, a marginally significant difference ( $p < 0.1$ ) was found for turbidity. Turbidity concentrations were highest in the transition zone between the cropland zone and the shrubland zone. When evaluated over time, monthly Chl-a and turbidity steadily decreased from 2019 to 2022. Notably, Chl-a concentrations declined at a significantly greater rate in the cropland zone than within the shrubland zone. When accounting for seasonal fluctuations in water quality, approximately 40% of reservoirs displayed significantly decreasing trends in Chl-a, more than half of which were in the cropland zone. Furthermore, turbidity declined in 32% of reservoirs. Additionally, I found a quarter of all reservoirs in this study dried out completely and almost half of all reservoirs lost more than 50% of their surface area. Areal loss was highest in the cropland zone, likely due to a higher number of users and relative ease of access.

### 3.2 Model Comparisons Demonstrate the Utility of Sentinel-2 and PlanetScope

My findings confirm the trade-offs and benefits seen in other semi-empirical approaches to water quality retrieval related to spatial and spectral resolution when estimating Chl-a and turbidity. For example, in Oklahoma Sentinel-2 satellites were better at estimating Chl-a ( $R^2 = 0.86$ ), whereas PlanetScope satellites were better at estimating turbidity ( $R^2 = 0.87$ ) (Mansaray et al., 2021). Similarly, I found that the top Chl-a model using Sentinel-2 satellites explained slightly more variation ( $R^2 = 0.69$ ,  $P = 4.2E-06$ ) compared to the Planet satellites ( $R^2 = 0.67$ ,  $P = 3.1E-05$ ). Although Planet satellites offer a higher spatial resolution, the actual onboard sensors were limited in the number of bands captured compared to the Sentinel-2 MSI sensor which offers 12 narrow spectral bands. The addition of Red-Edge bands (~700-780nm) in the Sentinel-2 imagery allowed for the use of more indices such as NDCI, SABI, Three-Band Algorithm, and the Maximum Chlorophyll Index (MCI). NDCI and the RedEdge to Red Algorithms were both significant in the top Sentinel-2 models and explained more variation in the Chl-a models through the Red-Edge bands. Conversely, the spectral data from the Planet satellites explained more variation in the turbidity models ( $R^2 = 0.72$ ,  $P = 7.2E-05$ ) compared to the Sentinel-2 models ( $R^2 = 0.68$ ,  $P = 8.6E-05$ ). This is possibly due to the fact that many of the turbidity models centered around the Near Infrared wavelengths, which are completely absorbed in clear water with high reflectance in turbid waters. In this sense, both satellites were using the same wavelengths to estimate turbidity, however PlanetScope offered a much higher spatial resolution and a wider NIR band. Overall, the top turbidity model with an  $R^2 = 0.72$  performed as well or better than other published turbidity models that only used remote sensing indices. For example, geospatial mapping of turbidity concentrations using Sentinel-2 in the Chebara dam in Kenya achieved an  $R^2$  value of 0.7 (Ouma et al., 2018). Furthermore, when compared to coastal

turbidity models, my model results outperformed several others. For example, Planet imagery was only able to explain 41% of the variation in turbidity retrieval models in coastal regions around San Francisco and the United Kingdom (Vanhellemont, 2019). Additionally, turbidity maps in the Gulf of Gabes (Tunisia) using Sentinel-2 achieved  $R^2$  values close to 0.7 (Katlane et al., 2020). Conversely my top Chl-a model with an  $R^2= 0.69$  behaved similarly or slightly worse than other published Chl-a models based solely on remote sensing indices. For example, again in Kenya's Chebara dam, Chl-a achieved  $R^2$  value of 0.7 (Ouma et al., 2018). Additionally, retrievals of Chl-a from Estonian lakes using Sentinel-2 imagery achieved  $R^2$  values ranging from 0.2 to 0.95 (Ansper & Alikas, 2019). Models of Chl-a in lakes within agricultural watersheds achieved an  $R^2$  value of 0.85 (Mansaray et al., 2021). Additionally, a novel Normalized Difference Chlorophyll Index (NDCI) explained Chl-a with coefficients of determination up to 0.95 (Mishra & Mishra, 2012).

### **3.3 Landscape Features Helped Improve Water Quality Models**

Landscape features were significant in all models and enabled better estimations ( $R^2$  values 4 to 9% higher) for both Chl-a and turbidity than models using remote sensing indices alone.

Relevant features included percent landcover, specifically the proportion of forest, grassland, built area, and water within 100m of each reservoir. Landscape ecology and management has long operated under the premise that the spatial configuration and pattern of landscape features can help predict ecological processes (Baskent & Jordan, 1995; Gustafson, 1998), particularly for water quality (Gergel et al. 2001). For example, strong associations have been found between the amount of urban area and decreased water quality (Carpenter et al., 1998; Gorgoglione et al., 2020; Mello et al., 2018, 2020). In this study, the proportion of built area was significant in

global Chl-a estimations (partial  $R^2 = 0.1$ ) and was inversely related to water quality. Large amounts of nonpermeable surfaces are common in urban landcovers, and are associated with excess runoff after precipitation events which likely reduces overall water quality (Ferreira et al., 2016; Huang & Gergel, 2022; Ruan et al., 2019; Walsh et al., 2012).

Furthermore, increased vegetation (and specifically forests) within watersheds are repeatedly found to be strongly associated with improved water quality (Gorgoglione et al., 2020; Mello et al., 2020). I found forested land cover was significant in both Chl-a and turbidity models. In fact, across all models, the proportion of forests within 100m was the most influential landscape feature, explaining 30% of the variation in turbidity models. However, increased forest cover was associated with decreased water quality. This relationship between forest cover and water quality is counterintuitive, as increased forest cover generally reduces overland runoff after precipitation by enhancing infiltration into the soil column (Borrelli et al., 2017; Bradshaw et al., 2007; Liu et al., 2015) and in turn can reduce sedimentation in reservoirs. However, many studies quantifying the relationship forests have on erosion and flow regime are often based on temperate forests before and after logging activities. The forests in this study are predominantly naturally occurring sparse woodlands, with no history of logging activities. Therefore, sparse forests, characterized by considerably less trees, may not be stabilizing the soil in a comparable way. Thus, landscape indicators (such as the proportions of forests, built areas, and grasslands) (Gergel et al., 2002) may aid in estimations of Chl-a and turbidity by characterizing the role such land covers play in influencing runoff into reservoirs.

Other significant landscape features included maximum reservoir size and proximity to roads, both of which were most influential in turbidity models (partial  $R^2 = 0.13$  and  $0.21$  respectively). The negative effects of roads on sedimentation in water bodies are well documented (Forsyth et al., 2006; McGrane, 2016; Wemple et al., 2017), and often associated with an increase of impermeable surfaces (Walsh et al., 2012). Runoff generation can often carry a large variety of contaminants such as nutrients, fecal coliforms, heavy metals, oils, lubricants, and paints which end up in water bodies (Awonaike et al., 2022; Huang & Gergel, 2022; Tong & Chen, 2002). Additionally, the removal of vegetation along roads during construction (Castillo et al., 1997; Ramos-Scharrón & MacDonald, 2005), further increases the mobilization of sediment into the water bodies. In my models, reservoirs closer to roads were associated with worse water quality. The size of reservoirs was significant in water quality models, demonstrating that larger reservoirs were also associated with worse water quality. The mechanisms by which reservoir size is associated with water quality is unclear, however it is likely due to the tendency to build larger reservoirs closer to roads for accessibility. Reservoir size was inversely related to distance to roads, suggesting that larger reservoirs are indirectly associated with decreased water quality through their proximity to roads.

### **3.4 Regional Spatio-Temporal Trends in Water Quality Across a Land-Use Gradient**

Using the model derived estimates of water quality for 60 reservoirs, I found Chl-a concentrations were not statistically different across the land-use gradient and I found only a marginally significant ( $P < 0.10$ ) difference in turbidity. Elevated turbidity in the transition zone was largely counterintuitive, as this zone has the highest % forest cover, and erosion after precipitation is often lower in forested areas due to the greater soil infiltration (Borrelli et al., 2017; Bradshaw et al., 2007; Liu et al., 2015). However, the transition zone is situated

approximately 107 meters lower in elevation compared to the cropland zone and could therefore be experiencing a higher volume of excess overland runoff leading to higher levels of sedimentation.

In 2015, an assessment of the water quality in various rivers, water tanks and small reservoirs in Narok found that most water quality parameters complied with WHO water quality standards (Augustine et al., 2015). While the water quality units in this study cannot be directly compared to those used by the WHO, my results provide further evidence in support of improving water quality in reservoirs. Although mean and median Chl-a concentrations were similar across the land-use gradient, a finer analysis of temporal trends yielded two interesting insights. First, I found that water quality improved in most reservoirs from 2019-2022. More specifically, over 43 consecutive months Chl-a declined in 28 reservoirs, and furthermore, did not increase in any over this time period. Additionally, 24 reservoirs displayed significant declines in turbidity, whereas only 6 reservoirs exhibited increasing turbidity over the study period (2019-2022).

Second, the magnitude of change in Chl-a over this time differed along the land-use gradient. Importantly, the magnitude of change in Chl-a concentrations was significantly different across the land-use gradient when comparing Theil-Sen estimates. Chl-a concentrations declined more steeply in the cropland zone than the shrubland zone from 2019 to 2022. I hypothesize that this may be the result of recent changes in both fertilizer use as well as precipitation. Narok county is known as the wheat basket of Kenya, producing approximately half of Kenya's wheat during any given year (Ministry of Agriculture, Livestock, Fisheries, and Cooperatives Data Portal 2018). Highland wheat and barley are planted in the high elevation areas surrounding the Mau Forest

(the cropland zone). Commonly, fertilizer reaches water bodies after multiple precipitation events (Walsh, Fletcher, & Burns, 2012). Fertilizer shortages began in 2019/2020 in response to sustained high energy prices. These supply shocks led to sharp increases in the price of fertilizer in 2021 across Kenya, which possibly resulted in less inputs. In Narok, the marked decline in average precipitation since 2018 (Funk et al., 2015) likely further reduced the amount of fertilizer that reached small water bodies. Furthermore, the marked decline in precipitation has likely led to less erosion, and therefore less sedimentation in reservoirs.

### **3.5 Tracking Seasonal Shifts in Reservoir Size**

Tracking the changing boundaries of waterbodies is critical to understanding their seasonal dynamics and can be especially helpful in monitoring and mitigating the effects of floods and droughts. Boundary delineation often uses satellite imagery in multiple ways. Conventionally, enhanced water and soil moisture indices are created using satellite imagery at multiple timesteps to visualize change over several seasons (Ismail et al., 2022; Tangdamrongsub et al., 2021; Yue & Liu, 2019). These methods are efficient but are susceptible to reduced accuracies due to mixed pixel effects, which occur when boundary pixels exhibit properties of both water and land surfaces. The mixed pixel issue has occasionally been addressed using a series of algorithms which cluster pixels in intuitive ways (Sivasankari & Jayalakshmi, 2021), however it is more common to use image segmentation and classification combined with higher resolution satellite imagery (Mason et al., 2012).

Although numerous methods exist for boundary delineation, I was unable to successfully execute these methods due to the extremely small size of the reservoirs in this study. Much of the

research on boundary delineation for flood mapping relies on a small number of relatively large surface water bodies (Bagli & Soille, 2004; Brown & Young, 2006) . Any issues arising from mixed pixels (Hsieh et al., 2001) and cloud cover are marginal in comparison to the size of the water body. In the case of small water bodies, issues arising from cloud cover and mixed pixels are much more detrimental to the final product. Furthermore, the reflectance values of shoreline pixels are widely different across 60 reservoirs situated in different land-use contexts, making the task even more difficult. I therefore elected to manually digitize the boundaries of water bodies and forgo any automatic process.

During 2021 and 2022 alone, key community water pans in similar counties of Kilifi and Garissa have dried up (Astariko, 2021; County, 2021; Odiwuor, 2022). In Narok, I found approximately 25% of the 60 reservoirs fully dried out during the peak dry months (December), and nearly half (46%) of reservoirs lost more than 50% of their surface area. When viewed as a percentage change, the amount of change in the size of reservoirs was significantly different amongst the three land-use zones. Reservoirs in the cropland zone lost the most surface area (approximately 58% of their combined surface area) between the wet season and the dry seasons. However, when viewed on a proportional basis, the proportional change in area between the peak wet season (June) and the peak dry season (Dec) showed no significant differences across the three zones (Figure 8).

A higher number of water users combined with the relative ease of access could explain the higher areal loss in reservoirs in the cropland zone. Across the established land-use gradient, settled communities tend to be closer to agricultural lands, and the capital Narok town is only 10

highway km away from the cropland zone. Therefore, reservoirs in the cropland zone are potentially accessed by more people than reservoirs in the transition and shrubland zones. In a deeper analysis of the road network, I found that mean distance of reservoirs to the nearest main road was 146 m in the cropland zone compared to 340 m and 302 m in the transition and shrubland zones, respectively. Additionally, reservoirs located in the cropland zone were slightly larger on average (mean 3,104 m<sup>2</sup>) in comparison to the transition and shrubland zones (mean of 2,141 m<sup>2</sup> and 2,835 m<sup>2</sup>, respectively).

### **3.6 Limitations**

#### **3.6.1 Spatial Scale and Resolution of Available Information**

The mapped resolution for water quality constituents is likely too coarse to accurately capture minute spatial changes in water quality within the boundaries of such small reservoirs, especially so for Sentinel-2 imagery. The 10-meter spatial resolution offered by Sentinel-2, while considered high spatial resolution for many applications, is too coarse to quantify the water quality of even smaller water bodies and reservoirs which are abundant in Kenya. I tried to balance this limitation by specifically choosing reservoirs that were big enough to comprise many pixels. Future research must be pragmatic in choosing reservoirs of the sufficient size to maximize the use of a given satellite sensor.

Furthermore, satellites with multispectral sensors, such as those found on Sentinel-2 and PlantScope satellites, do not have the capability to measure the volume of water bodies.

Volumetric measurements of reservoirs are important to consider when estimating water quality and water loss. To account for this, I visually inspected all images taken of the reservoirs to

categorize them based on whether the reservoir was hand-dug or machine-excavated. Hand-dug reservoirs were shallow, whereas machine-excavated reservoirs were deep. This classification was used as a proxy for volume and included as a categorical variable during model-building.

Moreover, the Open Street Map (OSM) data is outdated and does not include information on smaller roads. The OSM dataset was first created for the region by Kenya's Department of Surveys in 2007 and does not represent the current network of roads and highways in Narok. Furthermore, the dataset focuses on large, paved roads and excludes information on small dirt roads that are popular in the region. The lack of comprehensive and up-to-date road data could confound results by misrepresenting the proximity of some reservoirs to roads.

In addition, the 2020 land cover map used here created by ESRI uses a deep learning model to classify images using an object-based classifier. Despite achieving an overall accuracy of 85% (Karra et al., 2021), the ESRI map is a global dataset not optimized for distinguishing between classes. Specifically, the limitation of the ESRI land cover map for my research is its inability to distinguish among different crop-types and their state of fallow. For example, row-crops such as wheat and barley would differ in the amount and timing of fertilizer applied throughout the seasons in comparison to sugarcane and tea. Furthermore, a field that has been left to fallow would receive no fertilizer inputs in comparison to field currently in use. Distinguishing among crops and states of fallow would offer more information on the timing and amount of fertilizer applied, as well as the harvest schedule. Taken together, these differences would in turn influence the effects of land cover on water quality and subsequent water quality estimations. Distinguishing between crop types using pixel and object-based classification can be difficult but

has been successfully achieved using various vegetation indices (Conrad et al., 2010; Peña-Barragán et al., 2011; Tommaso et al., 2021; K. F. Yang et al., 2020), albeit at a much smaller scale than the ESRI map.

The ESRI land cover map also demonstrated high levels of class confusion between grasslands and shrublands (Karra et al., 2021). Grasslands received a user's accuracy of around 38% in arid regions such as California and were commonly misclassified as shrubland. Although such errors are potentially significant, I believe they did not impact my research as I was primarily interested in the effects of forests and croplands on water quality. In this regard the classifier worked well, with forested and agricultural land covers achieving user's accuracies approaching 90% in arid regions.

Finally, it should be noted that the ESRI land cover map represents a static snapshot of a dynamic landscape. Fallowed croplands, or the conversion from forest to cropland, or shrubland to urban areas are all common land-use transitions in Narok. Although the land cover map was current at the beginning of this study (2020), the in-situ water quality measurements recorded in the field were not taken until late 2021 and early 2022. Therefore, it is possible that some areas of the landscape switched cover types over the study period. Land covers within 100m of each reservoir (used as variables in the model building) may no longer be accurate and could lead to inaccurate estimates of water quality. These errors could be remedied in future studies by using up-to-date land cover maps that coincide with the dates of in situ sampling.

### 3.6.2 Cloud Cover and Atmospheric Correction

Another limitation involves the extent of cloud cover in each image, images which were collected near the end of each month, close to the day of sampling. Certain months were naturally cloudier, impacting the imagery retrieved for those periods, potentially confounding the results and returning misleading estimations of both Chl-a and turbidity. To account for this, the supplemental scene classification maps provided with each Sentinel-2 image were used to mask out dense cloud pixels, which in turn returned NA values for cloudy reservoirs. All NA values were then omitted from subsequent analyses. However, low cloud cover pixels were not included in the supplemental scene classification maps and therefore any reservoirs with slightly cloudy pixels directly above were still used to calculate Chl-a and turbidity, potentially impacting my results.

Additionally, it is common practice in semi-empirical studies to acquire unprocessed imagery and apply atmospheric corrections manually using a suite of different algorithms (Ansper & Alikas, 2019; Pahlevan et al., 2020; Toming et al., 2016). The purpose is to test multiple atmospheric corrective algorithms and choose one which offers the strongest models based on the geographic location and imagery. I instead elected to use the generic Copernicus' Sentinel-2 Atmospheric Correction (S2AC) algorithm (Richter et al., 2011) to increase the speed of water quality retrieval within our workflow. Testing multiple algorithms could have made our models more robust by choosing an atmospheric correction that is optimized for semi-arid regions and therefore provide more accurate Bottom-of-atmosphere reflectance values.

### **3.6.3 Challenges During a Global Pandemic**

Finally, it should be noted that this study was conducted during a global pandemic caused by the Covid-19 virus. Like other countries, the Kenyan government responded through a series of lockdowns and restrictions. Such difficulties impacted the study directly by pushing back our intended sampling dates and were combined with import restrictions on our sampling equipment. The pandemic also directly and indirectly affected the way in which small businesses, farmers, and communities normally operated and behaved. At the beginning of 2020, Kenya had experienced three consecutive below-average rainy seasons which led to poor livestock and crop productions. Decreased food production coupled with the onset of the global Covid-19 pandemic drove staple food prices higher (Famine Early Warning Systems Network, n.d.; IPC Acute Food Insecurity, 2022). Additionally, in response to the pandemic, the Kenyan government issued a temporary closure of livestock markets, which further suppressed trade in livestock. The combined effects of food prices and reduced livestock trade has likely affected the livelihoods of both farmers and pastoralists, in turn leading to atypical behaviour in terms of farming and reservoir usage.

## **3.7 Implications**

### **3.7.1 Implication to Remote Sensing Researchers**

Sentinel-2 is advisable for Chl-a monitoring, as the addition of the red-edge and SWIR bands can allow for the detection of chlorophyll in productive waters with high amounts of turbidity.

Sentinel-2 data is open source and products are easily accessible through the Copernicus Open Access Sentinel Hub. Providing high resolution data free of charge has allowed other researchers to use this imagery in a wide variety of cases, which has resulted in the creation of many

additional atmospheric corrective models that can be easily applied by the user for different scenarios (Ansper & Alikas, 2019; Pahlevan et al., 2020; Toming et al., 2016).

Planet products provide high spatial resolution imagery (3m) on a daily basis due to the sheer number of Dove satellites currently in orbit (Planet Team 2022). Imagery captured at such frequent intervals could allow for rapid real-time monitoring of small-scale reservoirs across the world. Planet imagery excels in its estimation of turbidity due to its high spatial resolution (3m). However, these satellites are limited in the number of bands they have available and can therefore not take advantage of certain RS band indices that need Red-Edge or SWIR bands. Planet imagery is a paid service, which requires a license to access and is therefore not advisable for professionals who may want to test its use for water quality monitoring. This barrier to entry may also mean these products have not been tested as rigorously for water quality retrieval.

Furthermore, future researchers should be careful when choosing waterbodies, as the Sentinel-2 imagery has a spatial resolution of around 10-60m depending on the bands used (Copernicus Sentinel data 2022, processed by ESA). This can result in poor results when estimating the water quality of small waterbodies. Additionally, Sentinel-2 has a temporal resolution of 5-10 days, which means monitoring the water quality of waterbodies cannot be done daily.

### **3.7.2 Implications for Management in Semi-Arid Regions**

These findings highlight both the significance and vulnerability of small-scale reservoirs in semi-arid regions. Funding for climate resilient infrastructure such as those from the Northeastern Development Initiative (NEDI) are vital for counties in the southwestern portion of Kenya as well. With a quarter of the reservoirs in our study drying out completely within months, I believe

funding for more reservoirs would benefit local communities as well as nomadic pastoral communities in the region.

The results of this study provide valuable context on reservoir management in semi-arid regions. The size and location of reservoirs heavily influences their propensity to dry-up, as well as their water quality. Specifically, I found that large reservoirs were less resilient to areal loss during the dry months (likely due to their excessive use) and were associated with higher turbidity.

Therefore, the size of new reservoirs should be carefully considered in order to reduce the combined effects of areal loss and decreased water quality. While reservoirs built near roads are more accessible, they are susceptible to increased turbidity and can sometimes be far away from nomadic pastoral communities moving through rural areas. Furthermore, it was found that reservoirs in grasslands had better (lower) Chl-a concentrations, whereas reservoirs near more urban land covers had worse (higher) Chl-a concentrations. Therefore, the proximity of reservoirs to roads and the land cover upon which they are built are two important factors to consider in order to reduce the effects of nonpermeable surfaces on water quality.

Across 3 years of consecutive sampling in 60 reservoirs, I found water quality has remained constant or improved in most reservoirs. These positive results highlight the relative stability of water quality in small-scale reservoirs, and further emphasizes the contributions these reservoirs can provide to water security under a changing climate.

### 3.8 Future Research

This study can and should be replicated to not only improve upon the water quality models, but to further analyse the effects of land cover on water quality. To begin with, further field measurements should be taken to ground truth our model-derived extrapolations to ensure the predictive power of our models. Furthermore, the TAL-PC and turbidity sensors used in this study measure Chl-a and turbidity in relative units which cannot be compared to the concentrations of international water quality standards. Converting relative units (eg: RFU) to concentrations (eg:  $\mu\text{g/L}$ ) can take place during the ground truthing, whereby a small sample is taken from each reservoir visited as part of the model-validation. The phytoplankton in each sample are then concentrated onto a fiber filter, and the cells mechanically ruptured. The chlorophyll is then extracted from the ruptured cells into an organic solvent (Acetone). The solution is once again filtered, and the remaining chlorophyll measured using a spectrophotometer. A simple correlation can then be built between the relative measurements taken using the sonde, and the concentrations derived in the lab. This correlation can then be programmed into the handheld sonde and used to retrieve Chl-a as a concentration during each site-visit. A similar process would need to be conducted separately to derive total suspended sediment (eg:  $\text{mg/L}$ ) from the relative turbidity units (NTU). Converting relative units to concentrations would allow future researchers to detect reservoirs which have fallen below international standards of water quality.

The models built for this study could be further improved upon by optimizing the imagery for semi-arid landscapes by attempting a suite of different atmospheric corrective algorithms and choosing the most appropriate one for the region. Additionally, large accuracy gains could be

met by simply increasing the sampling size and temporal range of the in-situ data, which would be especially helpful when using a semi-empirical approach to water quality estimation. Field samples which only assessed 12 reservoirs during December & January was the result of not accounting for reservoirs drying out and not being available for sampling. This further reduced the already low sample size for these months and made building a reliable model difficult and prone to over-fitting. Furthermore, evaluating a wider range of water quality parameters such as pH, dissolved oxygen, and fecal coliform would allow for a more nuanced and robust snapshot of the quality of the water.

Although our workflow for estimating water quality parameters from satellite imagery is semi-automatic and relatively quick, these benefits are not fully met by its use in an academic setting. Rather, incorporating our workflow within a citizen science project would allow small-scale farmers and pastoralists to retrieve a snapshot of their reservoir's water quality at any time using open-source satellite imagery. For example, the Plant Village app (developed at Penn State University) uses proprietary artificial intelligence to provide free estimates of crop health to farmers based on a few simple inputs by the user (Pennsylvania State University, 2022). Integrating our models within such a platform could be beneficial to farmers, pastoralists or any community interested in a free, non-invasive assessment of their water quality.

### **3.9 Significance and Conclusions**

Future climate scenarios are troubling in arid/semi-arid regions worldwide, making water management an increasingly vital consideration in every aspect of life. My goal with this research was to offer a data-driven approach to buffer against water-scarcity and drought by

improving the approaches for monitoring the status of reservoirs and help in optimizing the future placement of low-cost, climate resilient infrastructure in semi-arid regions. I found that small-scale reservoirs in Narok were severely vulnerable to seasonal weather fluctuations, with small and easily accessible reservoirs being the most vulnerable to drying out and reservoirs near forests being potentially the most vulnerable to water quality problems. Additionally, I found the water quality of small-scale reservoirs to be remarkably stable across time and across regions with differing land use, further emphasizing the effectiveness of these climate resilient waterbodies.

Geospatial data, tools, and techniques are evolving rapidly, and becoming more accessible and inexpensive. These technological changes make remote sensing a viable option in providing estimates of water quality under uncertain climate futures. This research has the potential to help build upon current approaches used in decision making within the water resources sector by further improving the monitoring of small-scale reservoirs. Furthermore, I believe a streamlined workflow for tracking the vulnerability of small inland waterbodies can be used to aid local communities and pastoralists in the arid and semi-arid regions across the globe.

## Literature Cited

- Ammenberg, P., Flink, P., Lindell, T., Pierson, D., & Strombeck, N. (2002). Bio-optical modelling combined with remote sensing to assess water quality. *International Journal of Remote Sensing*, 23(8), 1621–1638. <https://doi.org/10.1080/01431160110071860>
- Ansper, A., & Alikas, K. (2019). Retrieval of Chlorophyll a from Sentinel-2 MSI Data for the European Union Water Framework Directive Reporting Purposes. *Remote Sensing*, 11(1), Article 1. <https://doi.org/10.3390/rs11010064>
- Astariko, S. (2021, February 28). *Garissa faces severe water crisis as drought worsens*. [https://www.the-star.co.ke/counties/north-eastern/2021-02-28-garissa-faces-severe-water-crisis-as-drought-worsens/?utm\\_term=Autofeed&utm\\_medium=Social&utm\\_source=Facebook&fbclid=IwAR0lSNITHR9I5ZsB5xZqRvFIaxKiSJkeJzJo-9cu2t6G4gqVysk7\\_HskJ0o](https://www.the-star.co.ke/counties/north-eastern/2021-02-28-garissa-faces-severe-water-crisis-as-drought-worsens/?utm_term=Autofeed&utm_medium=Social&utm_source=Facebook&fbclid=IwAR0lSNITHR9I5ZsB5xZqRvFIaxKiSJkeJzJo-9cu2t6G4gqVysk7_HskJ0o)
- Augustine, A., Ndubi, D., Nathan, O., & Githae, E. (2015). *Determination of Physico-Chemical Properties Of Sources of Water In Narok North Sub-County, Kenya*. 4, 2319–1414.
- Awonaike, B., Parajulee, A., Lei, Y. D., & Wania, F. (2022). Traffic-related sources may dominate urban water contamination for many organic contaminants. *Environmental Research Letters*, 17(4), 044030. <https://doi.org/10.1088/1748-9326/ac5c0e>
- Bagheri, S. (2017). *Hyperspectral Remote Sensing of Nearshore Water Quality*. [https://doi.org/10.1007/978-3-319-46949-2\\_1](https://doi.org/10.1007/978-3-319-46949-2_1)
- Bagli, S., & Soille, P. (2004). *Automatic delineation of shoreline and lake boundaries from Landsat satellite images*.

- Baskent, E. Z., & Jordan, G. A. (1995). Characterizing spatial structure of forest landscapes. *Canadian Journal of Forest Research*, 25(11), 1830–1849. <https://doi.org/10.1139/x95-198>
- Bastviken, D., Tranvik, L. J., Downing, J. A., Crill, P. M., & Enrich-Prast, A. (2011). Freshwater Methane Emissions Offset the Continental Carbon Sink. *Science*, 331(6013), 50–50. <https://doi.org/10.1126/science.1196808>
- Beck, R., Xu, M., Zhan, S., Johansen, R., Liu, H., Tong, S., Yang, B., Shu, S., Wu, Q., Wang, S., Berling, K., Murray, A., Emery, E., Reif, M., Harwood, J., Young, J., Nietch, C., Macke, D., Martin, M., ... Huang, Y. (2019). Comparison of satellite reflectance algorithms for estimating turbidity and cyanobacterial concentrations in productive freshwaters using hyperspectral aircraft imagery and dense coincident surface observations. *Journal of Great Lakes Research*, 45(3), 413–433. <https://doi.org/10.1016/j.jglr.2018.09.001>
- Bonanse, M., Ledesma, M., Bazán, R., Ferral, A., German, A., O’Mill, P., Rodriguez, C., & Pinotti, L. (2019). Evaluating the feasibility of using Sentinel-2 imagery for water clarity assessment in a reservoir. *Journal of South American Earth Sciences*, 95, 102265. <https://doi.org/10.1016/j.jsames.2019.102265>
- Borrelli, P., Panagos, P., Märker, M., Modugno, S., & Schütt, B. (2017). Assessment of the impacts of clear-cutting on soil loss by water erosion in Italian forests: First comprehensive monitoring and modelling approach. *CATENA*, 149, 770–781. <https://doi.org/10.1016/j.catena.2016.02.017>
- Bradshaw, C. J. A., Sodhi, N. S., Peh, K. S.-H., & Brook, B. W. (2007). Global evidence that deforestation amplifies flood risk and severity in the developing world. *Global Change Biology*, 13(11), 2379–2395. <https://doi.org/10.1111/j.1365-2486.2007.01446.x>

- Bramich, J., Bolch, C. J. S., & Fischer, A. (2021). Improved red-edge chlorophyll-a detection for Sentinel 2. *Ecological Indicators*, *120*, 106876.  
<https://doi.org/10.1016/j.ecolind.2020.106876>
- Brewin, R., Smale, D., Moore, P., Dall’Olmo, G., Miller, P., Taylor, B., Smyth, T., Fishwick, J., & Yang, M. (2018). Evaluating Operational AVHRR Sea Surface Temperature Data at the Coastline Using Benthic Temperature Loggers. *Remote Sensing*, *10*(6), 925.  
<https://doi.org/10.3390/rs10060925>
- Brown, L., & Young, K. (2006). Assessment of Three Mapping Techniques to Delineate Lakes and Ponds in a Canadian High Arctic Wetland Complex. *Arctic*, *59*, 283–293.  
<https://doi.org/10.14430/arctic314>
- Bukata, R. (2013). Retrospection and introspection on remote sensing of inland water quality: “Like Déjà Vu All Over Again.” *Journal of Great Lakes Research*, *39*, 2–5.  
<https://doi.org/10.1016/j.jglr.2013.04.001>
- Bukata, R. P., Bruton, J. E., & Jerome, J. H. (1983). Use of chromaticity in remote measurements of water quality. *Remote Sensing of Environment*, *13*(2), 161–177.  
[https://doi.org/10.1016/0034-4257\(83\)90020-2](https://doi.org/10.1016/0034-4257(83)90020-2)
- Carpenter, S. R., Caraco, N. F., Correll, D. L., Howarth, R. W., Sharpley, A. N., & Smith, V. H. (1998). Nonpoint Pollution of Surface Waters with Phosphorus and Nitrogen. *Ecological Applications*, *8*(3), 559–568. [https://doi.org/10.1890/1051-0761\(1998\)008\[0559:NPOSWW\]2.0.CO;2](https://doi.org/10.1890/1051-0761(1998)008[0559:NPOSWW]2.0.CO;2)
- Castillo, V. M., Martinez-Mena, M., & Albaladejo, J. (1997). Runoff and Soil Loss Response to Vegetation Removal in a Semiarid Environment. *Soil Science Society of America Journal*, *61*(4), 1116–1121. <https://doi.org/10.2136/sssaj1997.03615995006100040018x>

- Chavula, G., Brezonik, P., Thenkabail, P., Johnson, T., & Bauer, M. (2009). Estimating chlorophyll concentration in Lake Malawi from MODIS satellite imagery. *Physics and Chemistry of the Earth, Parts A/B/C*, 34(13–16), 755.
- Chen, J., Zhang, M., Cui, T., & Wen, Z. (2013). A Review of Some Important Technical Problems in Respect of Satellite Remote Sensing of Chlorophyll-a Concentration in Coastal Waters. *IEEE Journal of Selected Topics in Applied Earth Observations and Remote Sensing*, 6(5), 2275–2289. <https://doi.org/10.1109/JSTARS.2013.2242845>
- Clarke, G. L., Ewing, G. C., & Lorenzen, C. J. (1970). Spectra of Backscattered Light from the Sea Obtained from Aircraft as a Measure of Chlorophyll Concentration. *Science*, 167(3921), 1119–1121. <https://doi.org/10.1126/science.167.3921.1119>
- Conrad, C., Fritsch, S., Zeidler, J., Rucker, G., & Dech, S. (2010). Per-Field Irrigated Crop Classification in Arid Central Asia Using SPOT and ASTER Data. *Remote Sensing*, 2(4), Article 4. <https://doi.org/10.3390/rs2041035>
- Coops, N. C., & Tooke, T. R. (2017). Introduction to Remote Sensing. In S. E. Gergel & M. G. Turner (Eds.), *Learning Landscape Ecology: A Practical Guide to Concepts and Techniques* (pp. 3–19). Springer. [https://doi.org/10.1007/978-1-4939-6374-4\\_1](https://doi.org/10.1007/978-1-4939-6374-4_1)
- County Government of Narok. (2018). *Narok Municipality Integrated Development Plan 2018-2023* [Development Plan].
- County, T. (2021, November 10). *Water crisis looming as key water pans drying up*. <https://thecounty.co.ke/water-crisis-looming-as-key-water-pans-drying-up/>
- Cracknell, A. P. (2017). UAVs: Regulations and law enforcement. *International Journal of Remote Sensing*, 38(8–10), 3054–3067. <https://doi.org/10.1080/01431161.2017.1302115>

- Dall'Olmo, G., & Gitelson, A. A. (2005). Effect of bio-optical parameter variability on the remote estimation of chlorophyll-a concentration in turbid productive waters: Experimental results. *Applied Optics*, *44*(3), 412–422.  
<https://doi.org/10.1364/AO.44.000412>
- de Groot, R., Brander, L., van der Ploeg, S., Costanza, R., Bernard, F., Braat, L., Christie, M., Crossman, N., Ghermandi, A., Hein, L., Hussain, S., Kumar, P., McVittie, A., Portela, R., Rodriguez, L. C., ten Brink, P., & van Beukering, P. (2012). Global estimates of the value of ecosystems and their services in monetary units. *Ecosystem Services*, *1*(1), 50–61. <https://doi.org/10.1016/j.ecoser.2012.07.005>
- Dekker, A. G., & Peters, S. W. M. (1993). The use of the Thematic Mapper for the analysis of eutrophic lakes: A case study in the Netherlands. *International Journal of Remote Sensing*, *14*(5), 799–821. <https://doi.org/10.1080/01431169308904379>
- Dekker, A. G., Vos, R. J., & Peters, S. W. M. (2001). Comparison of remote sensing data, model results and in situ data for total suspended matter (TSM) in the southern Frisian lakes. *Science of The Total Environment*, *268*(1), 197–214. [https://doi.org/10.1016/S0048-9697\(00\)00679-3](https://doi.org/10.1016/S0048-9697(00)00679-3)
- Dekker, A. G., Vos, R. J., & Peters, S. W. M. (2002). Analytical algorithms for lake water TSM estimation for retrospective analyses of TM and SPOT sensor data. *International Journal of Remote Sensing*, *23*(1), 15–35. <https://doi.org/10.1080/01431160010006917>
- Delegido, J., Urrego, P., Vicente, E., Sòria-Perpinyà, X., Soria, J. M., Pereira-Sandoval, M., Ruiz-Verdú, A., Peña, R., & Moreno, J. (2019). Turbidez y profundidad de disco de Secchi con Sentinel-2 en embalses con diferente estado trófico en la Comunidad

- Valenciana. *Revista de Teledetección*, 54, Article 54.  
<https://doi.org/10.4995/raet.2019.12603>
- Department of Economic and Social Affairs. (2019). *World Population Prospects 2019 | Volume II: Demographic Profiles* (p. 688). United Nations.  
<https://www.un.org/development/desa/pd/news/world-population-prospects-2019-0>
- Döll, P. (2009). Vulnerability to the impact of climate change on renewable groundwater resources: A global-scale assessment. *Environmental Research Letters*, 4(3), 035006.  
<https://doi.org/10.1088/1748-9326/4/3/035006>
- Downing, J. (2014). Limnology and oceanography: Two estranged twins reuniting by global change. *Inland Waters*, 4, 215–232. <https://doi.org/10.5268/IW-4.2.753>
- Famine Early Warning Systems Network. (n.d.). *Historic 2021/2022 drought in Kenya to drive high assistance needs through 2022*. Retrieved September 13, 2022, from <https://fews.net/east-africa/kenya/alert/december-20-2021>
- FAO. (2018). *Pastoralism in Africa's drylands: Reducing risks, addressing vulnerability and enhancing resilience* (pp. v–5). FAO.  
<https://www.fao.org/documents/card/en/c/CA1312EN/>
- FAO. (2020). *The State of Food and Agriculture 2020: Overcoming water challenges in agriculture*. FAO. <https://doi.org/10.4060/cb1447en>
- Ferreira, C., Walsh, R., Costa, M., Coelho, C., & Dinis Ferreira, A. (2016). Dynamics of surface water quality driven by distinct urbanization patterns and storms in a Portuguese peri-urban catchment. *Journal of Soils and Sediments*, 16. <https://doi.org/10.1007/s11368-016-1423-4>

- Food and Agriculture Organization. (2009). *High Level Expert Forum—How to Feed the World in 2050*.
- Forsyth, A. R., Bubb, K. A., & Cox, M. E. (2006). Runoff, sediment loss and water quality from forest roads in a southeast Queensland coastal plain Pinus plantation. *Forest Ecology and Management*, 221(1), 194–206. <https://doi.org/10.1016/j.foreco.2005.09.018>
- Friedman, J. H. (1984). *A Variable Span Smoother*. STANFORD UNIV CA LAB FOR COMPUTATIONAL STATISTICS. <https://apps.dtic.mil/sti/citations/ADA148241>
- Funk, C., Dettinger, M. D., Michaelsen, J. C., Verdin, J. P., Brown, M. E., Barlow, M., & Hoell, A. (2008). Warming of the Indian Ocean threatens eastern and southern African food security but could be mitigated by agricultural development. *Proceedings of the National Academy of Sciences*, 105(32), 11081–11086. <https://doi.org/10.1073/pnas.0708196105>
- Funk, C., Peterson, P., Landsfeld, M., Pedreros, D., Verdin, J., Shukla, S., Husak, G., Rowland, J., Harrison, L., Hoell, A., & Michaelsen, J. (2015). The climate hazards infrared precipitation with stations—A new environmental record for monitoring extremes. *Scientific Data*, 2(1), Article 1. <https://doi.org/10.1038/sdata.2015.66>
- G. Quibell. (1992). Estimating chlorophyll concentrations using upwelling radiance from different freshwater algal genera. *International Journal of Remote Sensing*, 13(14), 2611–2621. <https://doi.org/10.1080/01431169208904067>
- Gergel, S. E., Turner, M. G., Miller, J. R., Melack, J. M., & Stanley, E. H. (2002). Landscape indicators of human impacts to riverine systems. *Aquatic Sciences*, 64(2), 118–128. <https://doi.org/10.1007/S00027-002-8060-2>
- Giardino, C., Pepe, M., Brivio, P. A., Ghezzi, P., & Zilioli, E. (2001). Detecting chlorophyll, Secchi disk depth and surface temperature in a sub-alpine lake using Landsat imagery.

- The Science of the Total Environment*, 268(1–3), 19–29. [https://doi.org/10.1016/s0048-9697\(00\)00692-6](https://doi.org/10.1016/s0048-9697(00)00692-6)
- Gilerson, A. A., Gitelson, A. A., Zhou, J., Gurlin, D., Moses, W., Ioannou, I., & Ahmed, S. A. (2010). Algorithms for remote estimation of chlorophyll-a in coastal and inland waters using red and near infrared bands. *Optics Express*, 18(23), 24109–24125. <https://doi.org/10.1364/OE.18.024109>
- Gitelson, A. (1992). The Peak near 700nm on Radiance Spectra of algae and water: Relationships of its Magnitude and Position with Chlorophyll Concentration. *International Journal of Remote Sensing*, 13(17), 3367–3373.
- Gitelson, A. (1993). Reflectance Models for Quantifying Chlorophyll in Inland Waters. *Papers in Natural Resources*. <https://digitalcommons.unl.edu/natrespapers/233>
- Gitelson, A. A., Gurlin, D., Moses, W. J., & Barrow, T. (2009). A bio-optical algorithm for the remote estimation of the chlorophyll-a concentration in case 2 waters. *Environmental Research Letters*, 4(4). <https://doi.org/10.1088/1748-9326/4/4/045003>
- Gitelson, A. A., & Merzlyak, M. N. (1996). Signature Analysis of Leaf Reflectance Spectra: Algorithm Development for Remote Sensing of Chlorophyll. *Journal of Plant Physiology*, 148(3), 494–500. [https://doi.org/10.1016/S0176-1617\(96\)80284-7](https://doi.org/10.1016/S0176-1617(96)80284-7)
- Glibert, P., Anderson, D., Gentien, P., Granéli, E., & Sellner, K. (2005). The Global, Complex Phenomena of Harmful Algal Blooms. *Oceanography*, 18(2), 136–147. <https://doi.org/10.5670/oceanog.2005.49>
- Gons, H. J. (1999). Optical Teledetection of Chlorophyll a in Turbid Inland Waters. *Environmental Science & Technology*, 33(7), 1127–1132. <https://doi.org/10.1021/es9809657>

- Gordon, H. R., Brown, O. B., & Jacobs, M. M. (1975). Computed Relationships Between the Inherent and Apparent Optical Properties of a Flat Homogeneous Ocean. *Applied Optics*, *14*(2), 417–427. <https://doi.org/10.1364/AO.14.000417>
- Gordon, H. R., & Clark, D. K. (1980). Atmospheric effects in the remote sensing of phytoplankton pigments. *Boundary-Layer Meteorology*, *18*(3), 299–313. <https://doi.org/10.1007/BF00122026>
- Gordon, H. R., & Morel, A. Y. (1983). *Remote Assessment of Ocean Color for Interpretation of Satellite Visible Imagery: A Review* (Vol. 4). American Geophysical Union. <https://doi.org/10.1029/LN004>
- Gorgoglione, A., Gregorio, J., Ríos, A., Alonso, J., Chreties, C., & Fossati, M. (2020). Influence of Land Use/Land Cover on Surface-Water Quality of Santa Lucía River, Uruguay. *Sustainability*, *12*(11), Article 11. <https://doi.org/10.3390/su12114692>
- Gower, J., Doerffer, R., & Borstad, G. (1999). Interpretation of the 685 nm peak in water-leaving radiance spectra in terms of fluorescence, absorption and scattering, and its observation by MERIS. *International Journal of Remote Sensing*, *20*, 1771–1786. <https://doi.org/10.1080/014311699212470>
- Gustafson, E. (1998). Quantifying Landscape Spatial Pattern: What Is the State of the Art? *Ecosystems*, *1*, 143–156. <https://doi.org/10.1007/s100219900011>
- Han, L., & Rundquist, D. C. (1997). Comparison of NIR/RED ratio and first derivative of reflectance in estimating algal-chlorophyll concentration: A case study in a turbid reservoir. *Remote Sensing of Environment*, *62*(3), 253–261. [https://doi.org/10.1016/S0034-4257\(97\)00106-5](https://doi.org/10.1016/S0034-4257(97)00106-5)

- Heisler, J., Glibert, P., Burkholder, J., Anderson, D., Cochlan, W., Dennison, W., Gobler, C., Dortch, Q., Heil, C., Humphries, E., Lewitus, A., Magnien, R., Marshall, H., Sellner, K., Stockwell, D., Stoecker, D., & Suddleson, M. (2008). Eutrophication and Harmful Algal Blooms: A Scientific Consensus. *Harmful Algae*, 8(1), 3–13.  
<https://doi.org/10.1016/j.hal.2008.08.006>
- Hirsch, R. M., Slack, J. R., & Smith, R. A. (1982). Techniques of trend analysis for monthly water quality data. *Water Resources Research*, 18(1), 107–121.  
<https://doi.org/10.1029/WR018i001p00107>
- Hofste, R., Kuzma, S., Walker, S., Sutanudjaja, E., Bierkens, M., Kuijper, M., Faneca Sanchez, M., Van Beek, R., Wada, Y., Galvis Rodríguez, S., & Reig, P. (2019). Aqueduct 3.0: Updated Decision-Relevant Global Water Risk Indicators. *World Resources Institute*.  
<https://doi.org/10.46830/writn.18.00146>
- Hovis, W. A., & Leung, K. C. (1977). Remote Sensing of Ocean Color. *Optical Engineering*, 16, 158. <https://doi.org/10.1117/12.7972093>
- Hsieh, P.-F., Lee, L. C., & Chen, N.-Y. (2001). Effect of spatial resolution on classification errors of pure and mixed pixels in remote sensing. *IEEE Transactions on Geoscience and Remote Sensing*, 39(12), 2657–2663. <https://doi.org/10.1109/36.975000>
- Huang, J., & Gergel, S. E. (2022). Landscape indicators as a tool for explaining heavy metal concentrations in urban streams. *Landscape and Urban Planning*, 220, 104331.  
<https://doi.org/10.1016/j.landurbplan.2021.104331>
- Hunter, P., Tyler, A., & Willby, N. (2009). Using Remote Sensing to Aid the Assessment of Human Health Risks from Blooms of Potentially Toxic Cyanobacteria. *Environmental Science & Technology*, 43, 2627–2633. <https://doi.org/10.1021/es802977u>

- IPC Acute Food Insecurity. (2022). *Dry Spells, Poor Production Worsen Kenya Food and Nutrition Crises* (Integrated Food Security Classification).  
<https://reliefweb.int/report/kenya/kenya-asal-ipc-acute-food-insecurity-and-acute-malnutrition-analysis-february-june-2022>
- Ismail, M. A., Waqas, M., Ali, A., Muzzamil, M. M., Abid, U., & Zia, T. (2022). Enhanced index for water body delineation and area calculation using Google Earth Engine: A case study of the Manchar Lake. *Journal of Water and Climate Change*, 13(2), 557–573.  
<https://doi.org/10.2166/wcc.2021.282>
- Jenny, J.-P., Anneville, O., Arnaud, F., Baulaz, Y., Bouffard, D., Domaizon, I., Bocaniov, S. A., Chèvre, N., Dittrich, M., Dorioz, J.-M., Dunlop, E. S., Dur, G., Guillard, J., Guinaldo, T., Jacquet, S., Jamoneau, A., Jawed, Z., Jeppesen, E., Krantzberg, G., ... Weyhenmeyer, G. A. (2020). Scientists' Warning to Humanity: Rapid degradation of the world's large lakes. *Journal of Great Lakes Research*, 46(4), 686–702.  
<https://doi.org/10.1016/j.jglr.2020.05.006>
- Jensen, J. R. (2005). *Introductory digital image processing: A remote sensing perspective* (3rd ed). Prentice Hall.
- Jerlov, N. G. (1976). Marine Optics. In *Elsevier Oceanography Series* (Vol. 14, pp. 1–231). Elsevier. [https://doi.org/10.1016/S0422-9894\(08\)70789-X](https://doi.org/10.1016/S0422-9894(08)70789-X)
- Joshi, I. D., D'Sa, E. J., Osburn, C. L., Bianchi, T. S., Ko, D. S., Oviedo-Vargas, D., Arellano, A. R., & Ward, N. D. (2017). Assessing chromophoric dissolved organic matter (CDOM) distribution, stocks, and fluxes in Apalachicola Bay using combined field, VIIRS ocean color, and model observations. *Remote Sensing of Environment*, 191, 359–372.  
<https://doi.org/10.1016/j.rse.2017.01.039>

- Juliane, V., Wagnitz, P., Schmiester, J., & Hernandez, E. (2019). *Drought Crisis—The Global Thirst for Water in the Era of Climate Change* (pp. 1–17). World Wide Fund.  
[https://thewaternetwork.com/document-XAs/drought-crisis-the-global-thirst-for-water-in-the-era-of-climate-change-dHA1SPDe\\_s5IKWAOatdv1w](https://thewaternetwork.com/document-XAs/drought-crisis-the-global-thirst-for-water-in-the-era-of-climate-change-dHA1SPDe_s5IKWAOatdv1w)
- Kallio, K., Kutser, T., Hannonen, T., Koponen, S., Pulliainen, J., Vepsäläinen, J., & Pyhälähti, T. (2001). Retrieval of water quality from airborne imaging spectrometry of various lake types in different seasons. *The Science of the Total Environment*, 268(1–3), 59–77.  
[https://doi.org/10.1016/s0048-9697\(00\)00685-9](https://doi.org/10.1016/s0048-9697(00)00685-9)
- Karra, K., Kontgis, C., Statman-Weil, Z., Mazzariello, J. C., Mathis, M., & Brumby, S. P. (2021). Global land use / land cover with Sentinel 2 and deep learning. *2021 IEEE International Geoscience and Remote Sensing Symposium IGARSS*, 4704–4707.  
<https://doi.org/10.1109/IGARSS47720.2021.9553499>
- Katlane, R., Dupouy, C., Elkilani, B., & Berges, J. (2020). Estimation of Chlorophyll and Turbidity Using Sentinel 2A and EO1 Data in Kneiss Archipelago Gulf of Gabes, Tunisia. *International Journal of Geosciences*, VII, 708–728.  
<https://doi.org/10.4236/ijg.2020.1110035>
- Kendall, M. G. (1975). *Rank correlation methods* (4th ed., 2d impression). Griffin.
- Kirk, J. T. O. (1983). *Light and photosynthesis in aquatic ecosystems*. Cambridge University Press.
- Kowalczyk, P., Stoń-Egiert, J., Cooper, W. J., Whitehead, R. F., & Durako, M. J. (2005). Characterization of chromophoric dissolved organic matter (CDOM) in the Baltic Sea by excitation emission matrix fluorescence spectroscopy. *Marine Chemistry*, 96(3), 273–292. <https://doi.org/10.1016/j.marchem.2005.03.002>

- Kutser, T., Pierson, D. C., Kallio, K. Y., Reinart, A., & Sobek, S. (2005). Mapping lake CDOM by satellite remote sensing. *Remote Sensing of Environment*, 94(4), 535–540.  
<https://doi.org/10.1016/j.rse.2004.11.009>
- Lacaux, J. P., Tourre, Y. M., Vignolles, C., Ndione, J. A., & Lafaye, M. (2007). Classification of ponds from high-spatial resolution remote sensing: Application to Rift Valley Fever epidemics in Senegal. *Remote Sensing of Environment*, 106(1), 66–74.  
<https://doi.org/10.1016/j.rse.2006.07.012>
- Le, C. F., Li, Y. M., Zha, Y., Sun, D., & Yin, B. (2009). Validation of a Quasi-Analytical Algorithm for Highly Turbid Eutrophic Water of Meiliang Bay in Taihu Lake, China. *IEEE Transactions on Geoscience and Remote Sensing*, 47(8), 2492–2500.  
<https://doi.org/10.1109/TGRS.2009.2015658>
- Li, Y., Zhang, Y., Shi, K., Zhu, G., Zhou, Y., Zhang, Y., & Guo, Y. (2017). Monitoring spatiotemporal variations in nutrients in a large drinking water reservoir and their relationships with hydrological and meteorological conditions based on Landsat 8 imagery. *The Science of the Total Environment*, 599–600, 1705–1717.  
<https://doi.org/10.1016/j.scitotenv.2017.05.075>
- Liebmann, B., Hoerling, M. P., Funk, C., Bladé, I., Dole, R. M., Allured, D., Quan, X., Pegion, P., & Eischeid, J. K. (2014). Understanding Recent Eastern Horn of Africa Rainfall Variability and Change. *Journal of Climate*, 27(23), 8630–8645.
- Lillesand, T. M., & Kiefer, R. W. (1979). *Remote sensing and image interpretation*. Wiley.
- Lins, R. C., Martinez, J.-M., Motta Marques, D. D., Cirilo, J. A., & Fragoso, C. R. (2017). Assessment of Chlorophyll-a Remote Sensing Algorithms in a Productive Tropical

- Estuarine-Lagoon System. *Remote Sensing*, 9(6), Article 6.  
<https://doi.org/10.3390/rs9060516>
- Liu, W., Wei, X., Fan, H., Guo, X., Liu, Y., Zhang, M., & Li, Q. (2015). Response of flow regimes to deforestation and reforestation in a rain-dominated large watershed of subtropical China. *Hydrological Processes*, 29(24), 5003–5015.  
<https://doi.org/10.1002/hyp.10459>
- Lyapustin, A. I., Wang, Y., Laszlo, I., Hilker, T., G.Hall, F., Sellers, P. J., Tucker, C. J., & Korkin, S. V. (2012). Multi-angle implementation of atmospheric correction for MODIS (MAIAC): 3. Atmospheric correction. *Remote Sensing of Environment*, 127, 385–393.  
<https://doi.org/10.1016/j.rse.2012.09.002>
- Lyon, B., & DeWitt, D. G. (2012). A recent and abrupt decline in the East African long rains. *Geophysical Research Letters*, 39(2). <https://doi.org/10.1029/2011GL050337>
- Mann, H. B. (1945). Nonparametric Tests Against Trend. *Econometrica*, 13(3), 245–259.  
<https://doi.org/10.2307/1907187>
- Mansaray, A., Dzialowski, A., Martin, M., Wagner, K., Gholizadeh, H., & Stoodley, S. (2021). Comparing PlanetScope to Landsat-8 and Sentinel-2 for Sensing Water Quality in Reservoirs in Agricultural Watersheds. *Remote Sensing*, 13, 1847.  
<https://doi.org/10.3390/rs13091847>
- Marchetto, A. (2021). *rkt: Mann-Kendall Test, Seasonal and Regional Kendall tests* (1.6) [R].
- Mason, D., Davenport, I., Neal, J., Schumann, G., & Bates, P. (2012). Near Real-Time Flood Detection in Urban and Rural Areas Using High-Resolution Synthetic Aperture Radar Images. *Geoscience and Remote Sensing, IEEE Transactions On*, 50, 3041–3052.  
<https://doi.org/10.1109/TGRS.2011.2178030>

- Matthews, M. W. (2011). A current review of empirical procedures of remote sensing in inland and near-coastal transitional waters. *International Journal of Remote Sensing*, 32(21), 6855–6899. <https://doi.org/10.1080/01431161.2010.512947>
- McGrane, S. J. (2016). Impacts of urbanisation on hydrological and water quality dynamics, and urban water management: A review. *Hydrological Sciences Journal*, 61(13), 2295–2311. <https://doi.org/10.1080/02626667.2015.1128084>
- McLeod, A. I. (2022). *Kendall: Kendall Rank Correlation and Mann-Kendall Trend Test (2.2.1)* [R].
- Mello, K. de, Taniwaki, R. H., Paula, F. R. de, Valente, R. A., Randhir, T. O., Macedo, D. R., Leal, C. G., Rodrigues, C. B., & Hughes, R. M. (2020). Multiscale land use impacts on water quality: Assessment, planning, and future perspectives in Brazil. *Journal of Environmental Management*, 270, 110879. <https://doi.org/10.1016/j.jenvman.2020.110879>
- Mello, K. de, Valente, R. A., Randhir, T. O., dos Santos, A. C. A., & Vettorazzi, C. A. (2018). Effects of land use and land cover on water quality of low-order streams in Southeastern Brazil: Watershed versus riparian zone. *CATENA*, 167, 130–138. <https://doi.org/10.1016/j.catena.2018.04.027>
- Mishra, S., & Mishra, D. R. (2012). Normalized difference chlorophyll index: A novel model for remote estimation of chlorophyll-a concentration in turbid productive waters. *Remote Sensing of Environment*, 117, 394–406. <https://doi.org/10.1016/j.rse.2011.10.016>
- Morel, A., & Prieur, L. (1977). Analysis of variations in ocean color1: Ocean color analysis. *Limnology and Oceanography*, 22(4), 709–722. <https://doi.org/10.4319/lo.1977.22.4.0709>

- Mortimer, C. H. (1988). Discoveries and testable hypotheses arising from Coastal Zone Color Scanner imagery of southern Lake Michigan1. *Limnology and Oceanography*, 33(2), 203–226. <https://doi.org/10.4319/lo.1988.33.2.0203>
- Moses, W. J. (2009). *Satellite-based estimation of chlorophyll-a concentration in turbid productive waters* [Ph.D., The University of Nebraska - Lincoln].  
<https://www.proquest.com/docview/304941491/abstract/BD293FEC8CB345B9PQ/1>
- Moses, W. J., Gitelson, A. A., Berdnikov, S., & Povazhnyy, V. (2009). Satellite Estimation of Chlorophyll-a Concentration Using the Red and NIR Bands of MERIS—The Azov Sea Case Study. *IEEE Geoscience and Remote Sensing Letters*, 6(4), 845–849.  
<https://doi.org/10.1109/LGRS.2009.2026657>
- Nicholson, S. E. (2015). Long-term variability of the East African ‘short rains’ and its links to large-scale factors. *International Journal of Climatology*, 35(13), 3979–3990.  
<https://doi.org/10.1002/joc.4259>
- Odiwuor, K. (2022, March 20). Desperate for Water, Communities in Kenya’s Rural Areas Forced to Move. *Desperate for Water, Communities in Kenya’s Rural Areas Forced to Move*. <https://eastandhornofafrica.iom.int/stories/desperate-water-communities-kenyas-rural-areas-forced-move>
- Office for the Coordination of Humanitarian Affairs. (2022). *Horn of Africa Drought: Regional Humanitarian Overview & Call To Action* (p. 3). United Nations.  
<https://reliefweb.int/report/ethiopia/horn-africa-drought-regional-humanitarian-overview-call-action-published-4-july-2022>

- Olmanson, L., Bauer, M., & Brezonik, P. (2008). A 20-Year Landsat Water Clarity Census of Minnesota's 10,000 Lakes. *Remote Sensing of Environment*, *112*, 4086–4097.  
<https://doi.org/10.1016/j.rse.2007.12.013>
- O'Reilly, J. E., Maritorena, S., Mitchell, B. G., Siegel, D. A., Carder, K. L., Garver, S. A., Kahru, M., & McClain, C. (1998). Ocean color chlorophyll algorithms for SeaWiFS. *Journal of Geophysical Research: Oceans*, *103*(C11), 24937–24953.  
<https://doi.org/10.1029/98JC02160>
- Ouma, Y. O., Waga, J., Okech, M., Lavis, O., & Mbuthia, D. (2018). Estimation of Reservoir Bio-Optical Water Quality Parameters Using Smartphone Sensor Apps and Landsat ETM+: Review and Comparative Experimental Results. *Journal of Sensors*, *2018*, e3490757. <https://doi.org/10.1155/2018/3490757>
- Pahlevan, N., Smith, B., Schalles, J., Binding, C., Cao, Z., Ma, R., Alikas, K., Kangro, K., Gurlin, D., Hà, N., Matsushita, B., Moses, W., Greb, S., Lehmann, M. K., Ondrusek, M., Oppelt, N., & Stumpf, R. (2020). Seamless retrievals of chlorophyll-a from Sentinel-2 (MSI) and Sentinel-3 (OLCI) in inland and coastal waters: A machine-learning approach. *Remote Sensing of Environment*, *240*, 111604. <https://doi.org/10.1016/j.rse.2019.111604>
- Palmer, S. C. J., Kutser, T., & Hunter, P. D. (2015). Remote sensing of inland waters: Challenges, progress and future directions. *Remote Sensing of Environment*, *157*, 1–8.  
<https://doi.org/10.1016/j.rse.2014.09.021>
- Park, Y.-J., & Ruddick, K. (2005). Model of remote-sensing reflectance including bidirectional effects for case 1 and case 2 waters. *Applied Optics*, *44*, 1236–1249.  
<https://doi.org/10.1364/AO.44.001236>

- Peña-Barragán, J. M., Ngugi, M. K., Plant, R. E., & Six, J. (2011). Object-based crop identification using multiple vegetation indices, textural features and crop phenology. *Remote Sensing of Environment*, *115*(6), 1301–1316.  
<https://doi.org/10.1016/j.rse.2011.01.009>
- Pennsylvania State University. (2022). *PlantVillage Nuru*.  
[https://play.google.com/store/apps/details?id=plantvillage.nuru&hl=en\\_CA&gl=US](https://play.google.com/store/apps/details?id=plantvillage.nuru&hl=en_CA&gl=US)
- Petus, C., Chust, G., Gohin, F., Doxaran, D., Froidefond, J.-M., & Sagarminaga, Y. (2010). Estimating turbidity and total suspended matter in the Adour River plume (South Bay of Biscay) using MODIS 250-m imagery. *Continental Shelf Research*, *30*(5), 379–392.  
<https://doi.org/10.1016/j.csr.2009.12.007>
- Pohlert, T. (2020). *Trend: Non-Parametric Trend Tests and Change-Point Detection* (1.1.4) [R].
- Pörtner, H.-O., Roberts, D. C., Adams, H., Adelekan, I., Adler, C., Adrian, R., Aldunce, P., Ali, E., Begum, R. A., Bednar-Friedl, B., Bezner Kerr, R., Biesbroek, R., Birkmann, J., Bowen, K., Caretta, M. A., Carnicer, J., Castellanos, E., Cheong, T. S., Chow, W., ... Ibrahim, Z. Z. (2022). *Climate Change 2022: Impacts, Adaptation, and Vulnerability. Contribution of Working Group II to the Sixth Assessment Report of the Intergovernmental Panel on Climate Change* (No. 6; Technical Summary). IPCC.
- Preisendorfer, R. W. (1976). *Hydrologic Optics. Volume 1. Introduction* [Technical Report]. Honolulu : U.S. Dept. of Commerce, National Oceanic and Atmospheric Administration, Environmental Research Laboratories, Pacific Marine Environmental Laboratory.  
<https://udspace.udel.edu/handle/19716/1577>
- Prior, E. M., O'Donnell, F. C., Brodbeck, C., Runion, G. B., & Shepherd, S. L. (2021). Investigating small unoccupied aerial systems (sUAS) multispectral imagery for total

- suspended solids and turbidity monitoring in small streams. *International Journal of Remote Sensing*, 42(1), 39–64. <https://doi.org/10.1080/01431161.2020.1798546>
- R Core Team. (2022). *R: A Language and Environment for Statistical Computing*. R Foundation for Statistical Computing.
- Ramos-Scharrón, C. E., & MacDonald, L. H. (2005). Measurement and prediction of sediment production from unpaved roads, St John, US Virgin Islands. *Earth Surface Processes and Landforms*, 30(10), 1283–1304. <https://doi.org/10.1002/esp.1201>
- Ranghetti, L., Boschetti, M., Nutini, F., & Busetto, L. (2020). “sen2r”: An R toolbox for automatically downloading and preprocessing Sentinel-2 satellite data. *Computers & Geosciences*, 104473. <https://doi.org/10.1016/j.cageo.2020.104473>
- Rhee, D., Kim, Y., Kang, B., & Kim, D. (2017). Applications of unmanned aerial vehicles in fluvial remote sensing: An overview of recent achievements. *KSCE Journal of Civil Engineering*, 1–15. <https://doi.org/10.1007/s12205-017-1862-5>
- Richter, R., Schläpfer, D., & Müller, A. (2011). Operational Atmospheric Correction for Imaging Spectrometers Accounting for the Smile Effect. *IEEE Transactions on Geoscience and Remote Sensing*, 49(5), 1772–1780. <https://doi.org/10.1109/TGRS.2010.2089799>
- Rosegrant, M., Sulser, T., Mason-D’Croz, D., Nicola, C., Nin-Pratt, A., Dunston, S., Zhu, T., Ringler, C., Wiebe, Keith, D., Robinson, S., Willenbockel, D., Xie, H., Kwon, H.-Y., Johnson, T., Thomas, Timothy, S., Wimmer, F., Schaldach, R., Nelson, Gerald, C., & Willaarts, B. (2017). *Quantitative foresight modeling to inform the CGIAR research portfolio*. Intl Food Policy Res Inst.
- Ruan, X., Huang, J., Williams, D. A. R., Harker, K. J., & Gergel, S. E. (2019). High spatial resolution landscape indicators show promise in explaining water quality in urban

- streams. *Ecological Indicators*, 103, 321–330.  
<https://doi.org/10.1016/j.ecolind.2019.03.013>
- Ruiz-Verdu, A., Simis, S., De Hoyos, C., Gons, H., & Peña-Martínez, R. (2008). An evaluation of algorithms for the remote sensing of cyanobacterial biomass. *Remote Sensing of Environment*, 112, 3996–4008. <https://doi.org/10.1016/j.rse.2007.11.019>
- Salem, S. I., Higa, H., Kim, H., Kobayashi, H., Oki, K., & Oki, T. (2017). Assessment of Chlorophyll-a Algorithms Considering Different Trophic Statuses and Optimal Bands. *Sensors*, 17(8), Article 8. <https://doi.org/10.3390/s17081746>
- Sentinel User Handbook and Exploitation Tools. (2015). *Sentinel-2 User Handbook* (User Handbook No. 1; pp. 8–9). European Space Agency.  
[https://sentinels.copernicus.eu/web/sentinel/user-guides/document-library/-/asset\\_publisher/xlslt4309D5h/content/sentinel-2-user-handbook](https://sentinels.copernicus.eu/web/sentinel/user-guides/document-library/-/asset_publisher/xlslt4309D5h/content/sentinel-2-user-handbook)
- Shanmugam, P. (2012). CAAS: An atmospheric correction algorithm for the remote sensing of complex waters. *Annales Geophysicae*, 30(1), 203–220. <https://doi.org/10.5194/angeo-30-203-2012>
- Sibanda, M., Mutanga, O., Chimonyo, V. G. P., Clulow, A. D., Shoko, C., Mazvimavi, D., Dube, T., & Mabhaudhi, T. (2021). Application of Drone Technologies in Surface Water Resources Monitoring and Assessment: A Systematic Review of Progress, Challenges, and Opportunities in the Global South. *Drones*, 5(3), Article 3.  
<https://doi.org/10.3390/drones5030084>
- Siebert, S., Burke, J., Faures, J. M., Frenken, K., Hoogeveen, J., Döll, P., & Portmann, F. T. (2010). Groundwater use for irrigation – a global inventory. *Hydrology and Earth System Sciences*, 14(10), 1863–1880. <https://doi.org/10.5194/hess-14-1863-2010>

- Sivasankari, A., & Jayalakshmi, S. (2021). Land-use and Water body Delineation of Chennai and Kerala Lake with PSO, CSO and FCM. *2021 5th International Conference on Trends in Electronics and Informatics (ICOEI)*, 1763–1771.  
<https://doi.org/10.1109/ICOEI51242.2021.9452831>
- Smit, A. J., Roberts, M., Anderson, R. J., Dufois, F., Dudley, S. F. J., Bornman, T. G., Olbers, J., & Bolton, J. J. (2013). A Coastal Seawater Temperature Dataset for Biogeographical Studies: Large Biases between In Situ and Remotely-Sensed Data Sets around the Coast of South Africa. *PLOS ONE*, 8(12), e81944.  
<https://doi.org/10.1371/journal.pone.0081944>
- Soomets, T., Uudeberg, K., Jakovels, D., Brauns, A., Zagars, M., & Kutser, T. (2020). Validation and Comparison of Water Quality Products in Baltic Lakes Using Sentinel-2 MSI and Sentinel-3 OLCI Data. *Sensors*, 20(3), Article 3. <https://doi.org/10.3390/s20030742>
- Sun, D., Qiu, Z., Shi, K., & Shaoqi, G. (2014). Detection of Total Phosphorus Concentrations of Turbid Inland Waters Using a Remote Sensing Method. *Water Air and Soil Pollution*, 225. <https://doi.org/10.1007/s11270-014-1953-6>
- Tangdamrongsub, N., Forgotson, C., Gangodagamage, C., & Forgotson, J. (2021). The analysis of using satellite soil moisture observations for flood detection, evaluating over the Thailand's Great Flood of 2011. *Natural Hazards*, 108(3), 2879–2904.  
<https://doi.org/10.1007/s11069-021-04804-8>
- Tebbs, E. J., Remedios, J. J., & Harper, D. M. (2013). Remote sensing of chlorophyll-a as a measure of cyanobacterial biomass in Lake Bogoria, a hypertrophic, saline–alkaline, flamingo lake, using Landsat ETM+. *Remote Sensing of Environment*, 135, 92–106.  
<https://doi.org/10.1016/j.rse.2013.03.024>

- Toming, K., Kutser, T., Laas, A., Sepp, M., Paavel, B., & Nõges, T. (2016). First Experiences in Mapping Lake Water Quality Parameters with Sentinel-2 MSI Imagery. *Remote Sensing*, 8(8), Article 8. <https://doi.org/10.3390/rs8080640>
- Tommaso, S. D., Wang, S., & Lobell, D. B. (2021). Combining GEDI and Sentinel-2 for wall-to-wall mapping of tall and short crops. *Environmental Research Letters*, 16(12), 125002. <https://doi.org/10.1088/1748-9326/ac358c>
- Tong, S. T. Y., & Chen, W. (2002). Modeling the relationship between land use and surface water quality. *Journal of Environmental Management*, 66(4), 377–393. <https://doi.org/10.1006/jema.2002.0593>
- UNESCO World Water Assessment Programme. (2019). *UN World Water Development Report 2019: Leaving No One Behind*. United Nations Educational, Scientific and Cultural Organization. <https://www.unwater.org/publications/un-world-water-development-report-2019>
- United Nations. (2021). *The Sustainable Development Goals Report (Clean Water and Sanitation*, p. 13). <https://www.un.org/sustainabledevelopment/progress-report/>
- Vanhellemont, Q. (2019). Daily metre-scale mapping of water turbidity using CubeSat imagery. *Optics Express*, 27(20), A1372–A1399. <https://doi.org/10.1364/OE.27.0A1372>
- Vanhellemont, Q. (2020). Automated water surface temperature retrieval from Landsat 8/TIRS. *Remote Sensing of Environment*, 237, 111518. <https://doi.org/10.1016/j.rse.2019.111518>
- Verdin, J. P. (1985). *Monitoring Water Quality Conditions in a Large Western Reservoir with Landsat imagery*. 11.

- Walsh, C. J., Fletcher, T. D., & Burns, M. J. (2012). Urban stormwater runoff: A new class of environmental flow problem. *PloS One*, 7(9), e45814.  
<https://doi.org/10.1371/journal.pone.0045814>
- Wang, Y., Liu, D., Wang, Y., Gao, Z., & Keesing, J. K. (2019). Evaluation of standard and regional satellite chlorophyll-a algorithms for moderate-resolution imaging spectroradiometer (MODIS) in the Bohai and Yellow Seas, China: A comparison of chlorophyll-a magnitude and seasonality. *International Journal of Remote Sensing*, 40(13), 4980–4995. <https://doi.org/10.1080/01431161.2019.1577579>
- Water Services Regulatory Board. (2022). *A Performance Report of Kenya's Water Services Sector—2020/21* (No. 14; Impact). <https://wasreb.go.ke/impact-report-issue-no-14/>
- Wemple, B., Browning, T., Ziegler, A., Celi, J., Chun, K., Jaramillo, F., Leite, N., Ramchunder, S., Negishi, J., Palomeque, X., & Sawyer, D. (2017). Ecohydrological Disturbances Associated with Roads: Current Knowledge, Research Needs and Management Concerns with Reference to the Tropics. *Ecohydrology*, 11. <https://doi.org/10.1002/eco.1881>
- Williamson, C., Saros, J., Vincent, W., & Smol, J. (2009). Lakes and reservoirs as sentinels, integrators, and regulators of climate change. *Limnology and Oceanography*, 54.  
[https://doi.org/10.4319/lo.2009.54.6\\_part\\_2.2273](https://doi.org/10.4319/lo.2009.54.6_part_2.2273)
- Xu, M., Liu, H., Beck, R. A., Lekki, J., Yang, B., Liu, Y., Shu, S., Wang, S., Tokars, R., Anderson, R., Reif, M., & Emery, E. (2022). Implementation Strategy and Spatiotemporal Extensibility of Multipredictor Ensemble Model for Water Quality Parameter Retrieval With Multispectral Remote Sensing Data. *IEEE Transactions on Geoscience and Remote Sensing*, 60, 1–16. <https://doi.org/10.1109/TGRS.2020.3045921>

- Yang, H., Kong, J., Hu, H., Du, Y., Gao, M., & Chen, F. (2022). A Review of Remote Sensing for Water Quality Retrieval: Progress and Challenges. *Remote Sensing*, *14*(8), Article 8. <https://doi.org/10.3390/rs14081770>
- Yang, K. F., Gergel, S. E., Duriaux-Chavarría, J.-Y., & Baudron, F. (2020). Forest Edges Near Farms Enhance Wheat Productivity Measures: A Test Using High Spatial Resolution Remote Sensing of Smallholder Farms in Southern Ethiopia. *Frontiers in Sustainable Food Systems*, *4*. <https://www.frontiersin.org/articles/10.3389/fsufs.2020.00130>
- Yue, H., & Liu, Y. (2019). Method for delineating open water bodies based on the deeply clear waterbody delineation index. *Journal of Applied Remote Sensing*, *13*(3), 038504. <https://doi.org/10.1117/1.JRS.13.038504>

## Appendix

**Table A1 Summary of regression results explaining in-situ water quality as a function of Sentinel-2 remote sensing indices as well as other landscape variables (described in Figure 3). Chl-a and turbidity models using only month-specific data were contrasted to global models fit using in situ samples and satellite imagery for all months (Nov 2021 – Feb 2022). For each response variable, the 3 models with the lowest AIC values are shown. Top models (highlighted in grey below) were used for extrapolation of Chl-a and turbidity to a larger set of 60 reservoirs in the region and are explained in further detail in Table 5. An X indicates the variable was significant in the model, and an asterisk (\*) indicates variables that needed transformation.**

Water Quality Measure	n	Month	R <sup>2</sup>	Adj. R <sup>2</sup>	P-Value	Max VIF	AIC	NIR	Aerosol/Green	Blue/Green*	Blue/Red	Green/Blue	Green/Red	Red/Green	NIR/Red*	Red-Edge/Red	NDCI*	SABI	NDPI	NDTI	Three-Band-Algorithm	Dig Type	Road Proximity (m)*	Elevation (masl)	Maximum Size (m <sup>2</sup> )*	Built Area (%)*	Cropland (%)*	Grassland (%)*	Forest (%)*	Water (%)*				
<b>Chl-a (RFU)</b>																																		
max	30	Feb	0.69	0.64	4.2E-06	2.19	-	-	-0.83	-	-	-	-	-	-	3.69	-	-	-	-	-	-	-	-	-	-	-	-	-	-	-	-		
							-94.53	-	X	-	-	-	-	-	-	X	-	-	-	-	-	X	-	-	-	-	-	-	-	-	-	-		
							-94.05	-	X	-	-	-	-	-	-	X	-	-	-	-	-	X	-	-	-	-	-	-	-	-	-	-		
mean	30	Feb	0.58	0.56	1.1E-06	0.00	-	-	-	-	-	-	-	-	-	13.99	-	-	-	-	-	-	-	-	-	-	-	-	-	-	-	-		
							-95.63	-	-	-	-	-	-	-	-	X	X	-	-	-	-	-	-	-	-	-	-	-	-	-	-	-		
							-92.44	-	-	-	-	-	-	-	-	X	-	-	-	-	-	-	-	-	-	-	-	-	-	-	-	-		
max	77	all	0.54	0.50	1.0E-09	9.88	-	-	-0.53	-	-	-1.14	-	0.18	-0.25	-	17.30	-	-	-	-	-	-	-	-0.01	0.38	-	-	-	-	-	-		
							-196.85	-	X	X	-	X	-	X	X	-	X	X	-	-	-	X	-	-	X	X	-	-	-	-	-	-		
							-193.28	-	X	X	-	X	-	X	X	-	X	X	-	-	-	X	-	-	-	X	X	-	-	-	-	-	-	
mean	77	all	0.52	0.49	9.2E-11	1.75	-	-	-	-	-	-	-	-	-	9.93	-0.44	-	-	-	-	-	-	-	-	0.34	-	-	-	-	-	-		
							-197.05	-	-	-	-	-	-	X	X	X	X	X	-	-	X	-	-	-	-	X	-	-	-	-	-	-		
							-193.63	-	-	-	-	-	-	X	-	X	X	X	-	-	X	-	-	-	-	X	-	-	-	-	-	-	-	
<b>Turbidity (NTU)</b>																																		
mean	30	Feb	0.68	0.60	8.6E-05	1.54	-	4.90E-03	-	-	-5.58	-	-	-	-	-	-	-	-	-	-	-	-	-	-	-	-	-	-	-	-	-	-	
							75.93	X	-	-	X	-	-	-	-	-	-	-	-	-	-	-	-	-	-	-	-	-	-	-	-	-	-	
							76.74	X	-	-	X	-	-	-	-	-	-	-	-	-	-	-	-	-	-	-	-	-	-	-	-	-	-	-
max	30	Feb	0.60	0.50	8.5E-04	1.38	-	4.5E-03	-	-	-	-	-	-	-	-	-	-	-	-	17.91	-	-	-	-	-	-	-	-	-	-	-	-	
							92.96	X	-	-	-	-	-	-	-	-	-	-	-	-	X	-	-	-	-	-	-	-	-	-	-	-	-	-
							94.47	X	-	-	-	-	-	-	-	-	-	-	-	-	X	-	-	-	-	-	-	-	-	-	-	-	-	-
mean	77	all	0.49	0.47	4.2E-10	1.66	-	3.4E-03	-	-	-41.19	-	-	-	-	-	-	-	-	-	-	-	-	-	-	-	-	-	-	-	-	-	-	-
							272.89	X	-	-	X	-	-	-	-	-	-	-	-	-	-	-	-	-	-	-	-	-	-	-	-	-	-	-
							273.71	X	-	-	X	-	-	-	-	-	-	-	-	-	-	-	-	-	-	-	-	-	-	-	-	-	-	-
max	77	all	0.46	0.44	9.3E-10	1.71	-	0.004	-	-	-46.27	-	-	-	-	-	-	-	-	-	-	-	-	-	-	-	-	-	-	-	-	-	-	-
							294.00	X	-	-	X	-	-	-	-	-	-	-	-	-	-	-	-	-	-	-	-	-	-	-	-	-	-	-
							294.65	X	-	-	X	-	-	-	-	-	-	-	-	-	-	-	-	-	-	-	-	-	-	-	-	-	-	-

**Table A2 Summary of regression results explaining in-situ water quality as a function of PlanetScope remote sensing indices as well as other landscape variables (described in Figure 3). Chl-a and turbidity models using only month-specific data were contrasted to global models fit using in situ samples and satellite imagery for all months (Nov 2021 – Feb 2022). For each response variable, the 3 models with the lowest AIC values are shown. Top models (highlighted in grey below) were used for extrapolation of Chl-a and turbidity to a larger set of 60 reservoirs in the region and are explained in further detail in Table 5. An X indicates the variable was significant in the model, and an asterisk (\*) indicates variables that needed transformation.**

Water Quality Measure	n	Month	R <sup>2</sup>	Adj. R <sup>2</sup>	P-Value	Max VIF	AIC	Blue	Green	Red	Red <sup>3</sup>	NIR	Blue/Green*	Blue/Red	Green/Blue	Green/Red	Red/Green	NIR/Red*	Dig Type	Road Proximity (m)*	Elevation (masl)	Maximum Size (m <sup>2</sup> )*	Shrubland (%)*	Bare Ground (%)	Built Area (%)*	Cropland (%)*	Grassland (%)*	Forest (%)*	Water (%)*	
Chl-a (RFU)																														
mean	30	Feb	0.67	0.61	3.1E-05	3.51	-	-	-	-	-	-	-	-	0.11	1.08	-	-	-	-0.03	-	-	-1.7E-05	-0.14	-	-	-	-	-	-
							-87.98	-	-	-	-	-	-	-	X	X	-	-	-	X	-	-	X	X	-	-	-	-	-	
							-87.15	-	-	-	-	-	-	-	X	X	-	-	-	-	-	-	X	X	-	-	-	-	-	
max	30	Feb	0.71	0.60	2.9E-04	7.93	-	0.00	-	-	-	-	-	-	-	-	-	-	-	-0.03	-0.01	-	-	-0.16	0.32	5.4E-05	-	0.15	-	
							-92.55	X	X	-	X	-	-	-	-	-	-	-	-	X	X	-	-	X	X	X	-	X	-	
							-91.40	X	X	-	-	-	-	-	-	-	-	-	-	X	X	-	-	X	X	X	-	X	-	
max	77	all	0.46	0.39	8.3E-07	6.56	-	-	-5.2E-04	-	-	-	-	-	-	-	-	0.85	-	-	-0.01	0.03	-	-	0.31	5.8E-05	-	-	-1.38	
							-157.72	-	X	-	-	-	-	-	-	-	-	X	-	-	X	X	-	-	X	X	X	-	X	
							-157.59	-	X	-	-	-	-	-	-	-	-	X	-	-	X	X	-	-	X	X	-	-	X	
mean	77	all	0.44	0.36	6.1E-06	9.03	-	-	-	-6.3E-04	-	-	2.24	-	0.45	-1.05	-	-	-	-	-1.6E-03	0.04	-	-	0.36	-	-	0.06	-1.59	
							-165.24	-	-	X	X	-	X	-	X	X	-	-	-	-	X	X	-	-	X	-	-	X	X	
							-164.02	-	-	X	X	-	X	-	X	X	-	-	-	-	X	-	-	-	X	-	-	X	X	
Turbidity (NTU)																														
mean	30	Feb	0.72	0.63	7.2E-05	1.60	-	-	-	-	0.00	0.00	-	18.89	-	-	-	-	-	-0.60	-	0.44	-	-	-	-	-	2.66	8.69	
							74.03	-	-	-	X	X	-	X	-	-	-	-	-	X	-	X	-	-	-	-	-	X	X	
							75.79	-	-	-	X	X	-	-	-	-	-	-	-	X	-	X	-	-	-	-	-	X	X	
mean	77	all	0.66	0.63	4.2E-14	2.13	-	-	-	0.02	-	-	-	-	-	-	-	29.85	-	-0.53	-	-	0.00	1.62	-6.30	-	-	1.46	-	
							238.90	-	-	X	X	-	-	-	-	-	-	X	X	X	-	-	X	X	X	-	-	X	-	
							240.14	-	-	X	X	-	-	-	-	-	-	X	X	X	-	-	X	X	-	-	-	X	-	
max	30	Feb	0.59	0.51	3.9E-04	1.25	-	-	0.01	-	-	3.8E-03	-	-	-	-	-	-	-	-0.92	-	-	-	-	-	-	-	2.34	16.86	
							91.79	-	X	-	-	X	-	-	-	-	-	-	-	X	-	-	-	-	-	-	-	X	X	
							92.02	-	X	-	-	X	-	-	-	-	-	-	-	X	-	-	-	-	-	-	-	X	-	
max	77	all	0.56	0.53	4.3E-12	1.58	-	-	-	0.02	-	-	-	-	-	-	-	24.07	-	-0.59	-	-	-	-	-	-	-	2.19	-	
							267.83	-	-	X	X	-	-	-	-	-	-	X	-	X	-	-	-	-	-	-	-	X	-	
							273.44	-	-	X	X	-	-	-	-	-	-	X	-	-	-	-	-	-	-	-	-	X	-	

**Table A3 Summary of Mann-Kendall trend test results for all reservoirs exhibiting significant ( $p < 0.05$ ) trends. Top global models (Table 4, Figure 4) were used to make Chl-a and turbidity estimations for 60 reservoirs across 43 months (January 2019 – July 2022) and used to examine temporal trends in water quality. \* Indicates reservoirs with significant seasonal Mann-Kendall results (see Appendix A.4 for full list).**

<b>Reservoir ID</b>	<b>MK (tau)</b>	<b>MK (p-values)</b>	<b>Theil-Sen Slope</b>
<b>Chlorophyll-a Trends</b>			
103*	-0.56	1.06E-07	-1.11
112*	-0.51	1.48E-06	-0.54
110*	-0.45	1.96E-05	-0.42
122*	-0.44	3.41E-05	-1.07
105*	-0.42	6.39E-05	-0.31
368*	-0.39	2.30E-04	-0.25
412*	-0.38	4.04E-04	-1.01
229*	-0.37	4.73E-04	-0.27
418*	-0.35	1.02E-03	-0.84
119*	-0.34	1.47E-03	-0.31
355*	-0.33	1.95E-03	-0.10
117*	-0.32	2.41E-03	-0.43
410*	-0.32	2.76E-03	-0.09
225*	-0.31	3.39E-03	-0.13
375*	-0.30	4.72E-03	-0.14
345*	-0.30	5.04E-03	-0.22
100*	-0.30	5.37E-03	-0.18
352*	-0.27	1.20E-02	-0.11
109*	-0.26	1.43E-02	-0.29
120*	-0.26	1.61E-02	-0.81
405	-0.25	1.70E-02	-0.19
407*	-0.25	1.70E-02	-0.11
235*	-0.24	2.38E-02	-0.50
415	-0.24	2.38E-02	-0.20
413	-0.24	2.65E-02	-0.26
417*	-0.24	2.65E-02	-0.18
411	-0.22	4.02E-02	-0.14
409*	-0.21	4.68E-02	-0.14
<b>Turbidity Trends</b>			

243*	-0.71	1.59E-11	-27.87
100*	-0.60	1.91E-08	-9.27
237*	-0.59	2.43E-08	-19.80
405*	-0.55	2.21E-07	-10.69
401*	-0.53	5.06E-07	-15.29
396*	-0.52	9.66E-07	-11.84
223*	-0.50	2.75E-06	-25.87
241*	-0.47	9.50E-06	-10.85
393*	-0.46	1.47E-05	-7.48
109*	-0.44	2.83E-05	-7.93
244*	-0.41	1.17E-04	-16.03
418*	-0.40	1.39E-04	-5.42
222*	0.39	2.20E-04	8.04
395*	-0.38	3.44E-04	-15.70
408*	-0.38	4.04E-04	-6.26
352*	-0.37	4.37E-04	-3.72
101*	-0.35	1.05E-03	-6.07
364	-0.33	2.09E-03	-7.88
246*	-0.32	2.76E-03	-7.47
413*	0.31	3.06E-03	3.35
248*	-0.31	3.87E-03	-8.08
122*	0.30	5.54E-03	3.47
221*	-0.30	5.79E-03	-3.35
356	-0.29	6.30E-03	-7.00
118*	0.29	6.93E-03	5.99
224	-0.28	8.62E-03	-4.91
357	-0.25	1.70E-02	-5.45
412*	0.25	1.80E-02	3.50
409*	0.24	2.44E-02	4.00
419	-0.24	2.51E-02	-1.38

**Table A4 Summary of Seasonal Mann-Kendall trend test results for all reservoirs exhibiting significant ( $p < 0.05$ ) trends. Top global models (Table 4, Figure 4) were used to make Chl-a and turbidity estimations for 60 reservoirs across 43 months (January 2019 – July 2022) and used to examine temporal trends in water quality.**

Reservoir ID	p-value	Kendall Score	Slope	MK (Tau)
<b>Chlorophyll-a Trends</b>				
103	0.00	-171.00	-10.14	-0.56
112	0.00	-151.00	-6.31	-0.50
368	0.00	-151.00	-3.39	-0.50
122	0.00	-147.00	-15.67	-0.49
119	0.00	-139.00	-3.24	-0.46
110	0.00	-135.00	-4.97	-0.45
412	0.00	-129.00	-12.87	-0.43
410	0.00	-127.00	-1.61	-0.42
229	0.00	-123.00	-3.56	-0.41
117	0.00	-121.00	-5.97	-0.40
105	0.00	-113.00	-2.87	-0.37
100	0.00	-107.00	-2.93	-0.35
355	0.00	-107.00	-1.48	-0.35
225	0.01	-97.00	-1.40	-0.32
418	0.01	-97.00	-8.08	-0.32
375	0.01	-93.00	-1.74	-0.31
409	0.01	-93.00	-1.88	-0.31
345	0.01	-91.00	-3.07	-0.30
235	0.01	-89.00	-6.64	-0.29
352	0.02	-85.00	-1.45	-0.28
417	0.02	-85.00	-1.81	-0.28
120	0.02	-81.00	-10.64	-0.27
109	0.04	-75.00	-3.31	-0.25
407	0.04	-73.00	-1.18	-0.24
<b>Turbidity Trends</b>				
100	0.00	-159.00	-86.39	-0.52
243	0.00	-171.00	-313.68	-0.56
237	0.00	-153.00	-215.99	-0.50
241	0.00	-149.00	-115.48	-0.49
401	0.00	-146.00	-147.29	-0.48
405	0.00	-139.00	-100.38	-0.46
223	0.00	-136.00	-298.60	-0.45

396	0.00	-130.00	-116.73	-0.43
395	0.00	-120.00	-155.76	-0.40
244	0.00	-112.00	-165.91	-0.37
393	0.00	-110.00	-77.28	-0.36
352	0.00	-104.00	-42.57	-0.34
418	0.00	-104.00	-48.57	-0.34
109	0.00	-102.00	-73.80	-0.34
101	0.01	-99.00	-62.64	-0.33
408	0.01	-92.00	-57.25	-0.30
248	0.02	-86.00	-102.99	-0.28
221	0.03	-79.00	-36.06	-0.26
246	0.03	-76.00	-67.64	-0.25
417	0.04	74.00	21.94	0.24
103	0.03	76.00	30.07	0.25
413	0.03	79.00	37.63	0.26
412	0.01	90.00	50.84	0.30
222	0.01	91.00	76.06	0.30
409	0.01	97.00	58.57	0.32
118	0.00	100.00	87.94	0.33
122	0.00	127.00	58.39	0.42